HIGH-PERFORMANCE BRIDGE SYSTEMS FOR LIFELINE CORRIDORS IN THE PACIFIC NORTHWEST

PROJECT REPORT

by

Marc O. Eberhard
John F. Stanton
Hung V. Tran
Max T. Stephens
Dawn E Lehman
Charles W. Roeder

University of Washington

André R. Barbosa
David Trejo
Tim Link
Drew Nielson
Vandad Mazarei
Oregon State University

for
Pacific Northwest Transportation Consortium (PacTrans)
USDOT University Transportation Center for Federal Region 10
University of Washington
More Hall 112, Box 352700
Seattle, WA 98195-2700

DISCLAIMER

The contents of this report reflect the views of the authors, who are responsible for the facts and the accuracy of the information presented herein. This document is disseminated under the sponsorship of the U.S. Department of Transportation's University Transportation Centers Program, in the interest of information exchange. The Pacific Northwest Transportation Consortium and the U.S. Government assumes no liability for the contents or use thereof.

Technical Report Documentation Page

1. Report No.	2. Government Accession No.	3. Recipient's Catalog No.

4. Title and Subtitle HIGH-PERFORMANCE BRIDGE SYSTEMS FOR LIFELINE CORRIDORS IN THE PACIFIC NORTHWEST	**5. Report Date** 7/15/2015
7. Author(s) Marc O. Eberhard, John F. Stanton, Hung V. Tran, Dawn E Lehman, Charles W. Roeder, Max Stephens, André R. Barbosa, David Trejo, Tim Link, Dew Nielson, Vandad Mazarei	8. Performing Organization Report No. PACTRANS 12-03
9. Performing Organization Name and Address Pacific Northwest Transportation Consortium (PACTRANS) Oregon State University 101 Kearney Hall Corvallis, Oregon 97331 University of Washington More Hall 112, Box 352700 Seattle, WA 98195-2700	10. Work Unit No. (TRAIS) 11. Contract or Grant No.
12. Sponsoring Agency Name and Address Pacific Northwest Transportation Consortium (PACTRANS) University of Washington More Hall 112, Box 352700 Seattle, WA 98195-2700	13. Type of Report and Period Covered 14. Sponsoring Agency Code
15. Supplementary Notes	

16. Abstract

This report contributes to the development of three key strategies for increasing the seismic resilience of bridges, accelerating their construction, extending their lifespan, and decreasing life-cycle costs. The strategies considered were (1) precasting reinforced concrete columns, (2) constructing columns with concrete filled steel tubes (CSFTs), and (3) constructing columns with higher-strength steel (GR 80). The precast column strategy was furthered by conducting test of precast column to cast-in-place drilled shaft connections and developing a strut-and-tie model to proportion such connections. The strategy of using CFSTs was furthered by conducting tests of a variety of connections, which then provided the basis for design recommendations. The effect on seismic performance of using GR 80 steel was evaluated by performing four tests of columns and numerous material tests.

17. Key Words Seismic performance; accelerated construction, bridge, precast concrete, concrete-filled steel tube. reinforced concrete, high-strength steel	18. Distribution Statement No restrictions. Copies available from PACTRANS: www.pactrans.org		
19. Security Classification (of this report) Unclassified	20. Security Classification (of this page) Unclassified	21. No. of Pages	22. Price

EXECUTIVE SUMMARY

In current practice, nearly all bents (intermediate supports) are constructed of cast-in-place reinforced concrete and conventional reinforcing steel. Such bridges have served the Pacific Northwest (PNW) well in the past, but they need to be improved to meet current performance expectations. New strategies are needed to increase seismic resilience of bridges, accelerate their construction, and extend their lifespan (durability). This report contributes to the development of three key strategies for meeting these challenges, which would all lead to reduced life-cycle costs.

Precast Columns Supported by Drilled Shafts

A new type of connection between a precast concrete column and a drilled shaft has been developed for Accelerated Bridge Construction (ABC). The connection described in this report (Chapter 2) can be built quickly and allows generous placement tolerances. Three quasi-static large-scale tests of connections between a precast bridge column and a drilled shaft were performed to investigate the seismic performance of this connection.

The geometry of the test specimens was based on the minimum practical difference between the diameters of the shaft and the column, and so represented the most critical case. The performance of the system was investigated up to a drift ratio of 10%. The experimental results show that, if adequate confining steel is included in the splice zone, the plastic hinging mechanism forms in the column, without incurring damage in the splice zone or shaft. If the confinement is insufficient, the strength of the splice zone deteriorates rapidly with cyclic loading.

Concrete Filled Steel Tubes

Concrete filled steel tubes (CFSTs) are composite elements which consist of a steel tube with concrete infill, and offer an efficient alternative to conventional reinforced concrete construction, including rapid construction and reduced material and labor costs. However, the use of CFSTs in the US is limited in-part due to a lack of standard connection details.

This report focuses on the development of practical connections for CFSTs for use in moderate and high seismic regions with a specific emphasis on connections to precast concrete components. Two types of connections are being investigated, including column-to-foundation and column-to-cap beam connections. Extensive numerical parameter studies and experimental work resulted in straight forward design and corresponding expressions for a column-to-foundation connection in which the steel tube is embedded into the foundation concrete.

Development of the column-to-cap beam connection is more recent and is discussed in-depth here. This connection offers many unique design considerations including congested joint reinforcing and limits on geometry associated with the integration of precast super-structure components. Three categories of the CFST column-to-cap beam connection are being evaluated; an embedded connection similar to the proposed foundation connection, a connection in which headed reinforcing bars are welded to the inside of the steel tube and extended into the cap beam, and a traditional jacket RC connection in which a short independent cage of transverse and longitudinal column reinforcing extends from the steel tube into the cap beam (Chapter 4). All connections were developed and evaluated for use with precast bent caps for the optimization of accelerated bridge construction. Numerical and experimental results indicate that the proposed connection types can achieve adequate strength and ductility when subjected to extreme lateral loading. Design equations are provided in Chapter 5.

High Strength Steel for Reinforced Concrete Bridge Columns

In seismic regions, reinforcement congestion can present a significant challenge during construction of bridge structural members (Gustafson 2010; Risser and Hoffman 2014). One strategy for reducing this congestions is to use higher yield strength reinforcement, such as ASTM A706 Grade 80 [550] HSS reinforcement. Unfortunately, the lack of experimental testing results makes it difficult for bridge owners to have a sound support for designing members with such steel. Only limited research has been performed on the seismic performance on compression members constructed with HSS reinforcement.

Chapter 6 reports on testing performed on four half-scale circular RC bridge columns. Two pairs of columns were tested and evaluated to determine the effects of reinforcement grade and the effects of the moment-shear span ratio. Columns constructed with Grade 80 [550] HSS reinforcement achieved similar resistances when compared with the reference columns constructed with Grade 60 [420] reinforcement. All four columns failed due to longitudinal reinforcing bar buckling followed by longitudinal reinforcing bar fracture. Columns constructed with Grade 60 [420] reinforcement and columns constructed with Grade 80 [550] HSS reinforcement exhibited similar peak drift ratios. However, the columns constructed with Grade 60 [420] reinforcement exhibited larger hysteretic energy dissipation than the columns constructed with Grade 80 [550] HSS reinforcement. The reduction in the moment-shear span ratio did not affect the overstrength factor for columns constructed with either grade of reinforcement; results indicate that aspect ratio does not affect the overstrength factor for well detailed columns that do not exhibit shear failures.

Material tests on Grade 80 [550 MPa] tests, including additional monotonic tension testing of reinforcing steel bars from different manufacturers in the Pacific Northwest, low-cycle

fatigue testing of A615 and A706 Grade 80 [550 MPa] HSS reinforcement, and shear friction tests were also performed. These results results will be made available in a follow-up publication submitted to Oregon Department of Transportation in December 2015.

The results in this study present a promising step towards implementation of Grade 80 [550] HSS reinforcement in the design and construction of RC columns, within the bounds of the variables used in is testing program. Other parameters outside of the range studied in this paper should be evaluated. Those could include larger longitudinal reinforcement ratios, larger axial load ratios, and higher concrete strengths.

TABLE OF CONTENTS

CHAPTER 1

INTRODUCTION

The geometry, details and materials of newt bridges in seismic regions have changed little since the mid-1970s, when ductile details were first introduced into bridge engineering practice. Nearly all bents (intermediate supports) are constructed of cast-in-place reinforced concrete and conventional reinforcing steel. Such bridges have served the Pacific Northwest (PNW) well in the past, but to meet current performance expectations, new structural systems are needed to improve:

- *Seismic Resilience*. Improving seismic performance increases the safety of the travelling public, both by reducing the possibility of collapse and also, by allowing emergency vehicles to use the structure immediately following an earthquake.
- *Speed of Construction*. Reducing the onsite construction time further reduces the indirect costs of bridge construction. It also improves safety by reducing the amount of time that workers will be exposed to traffic hazards.
- *Durability*. The replacement of bridges can be costly and disruptive, so it is important that bridges last as long as possible.

To help address these challenges, the research described in this report furthers three strategies for improving the economy and performance of bridges located in the Pacific Northwest.

- *Precast Columns and Beams*. Precasting columns and cross-beams can accelerate the construction process onsite by moving time-consuming operations offsite. Previous research has considered the development of connections between precast column and

cross-beams (Pang et al., 2009), as well as precast columns and cast-in-place footings (Haraldsson et al., 2013). To provide a solution for bridges supported by deep foundation, this report describes three tests of connections between precast columns and drilled shafts (Chapter 2), and the development of a strut-and-tie model to proportion that connection (Chapter 3).

- *Concrete Filled Steel Tubes*. Concrete filled steel tubes (CFSTs) are composite elements which consist of a steel tube with concrete infill. These elements offer an efficient alternative to conventional reinforced concrete construction including rapid construction and reduced material and labor costs. However, the use of CFSTs in the US is limited in-part due to a lack of standard connection details. This report focuses on the development of practical connections for CFSTs for use in moderate and high seismic regions with a specific emphasis on connections to precast concrete components. Two types of connections are being investigated, including column-to-foundation and column-to-cap beam connections. Test of such connections are described in Chapter 4, and the design expressions are provided in Chapter 5.
- *High-Performance Reinforcement*. The availability of higher-strength reinforcing steel provides the opportunity to reduce construction costs and reinforcement congestion, which is a key concern in modern construction. Chapter 6 presents the results of a testing program developed to assess the performance of circular reinforced concrete (RC) bridge columns constructed with ASTM A706 Grade 80 [550] high-strength steel (HSS) reinforcement.

The strategies are compared with conventional cast-in-place construction in Chapter 7.

CHAPTER 2

EXPERIMENTS ON CONNECTIONS BETWEEN PRECAST CONCRETE COLUMNS AND DRILLED SHAFTS

2.1 INTRODUCTION

The use of cast-in-place columns in bridge construction requires long on-site construction times and large labor requirements in the field. Cast-in-place construction activities are particularly disruptive in situations in which they exacerbate traffic congestion (e.g., urban areas).

One strategy for reducing on-site construction time, field labor requirements, and traffic delays is to precast bridge elements offsite and assemble them together onsite. This strategy is already widely applied for bridge girders. In some cases, full bridges have been constructed off site and moved to the bridge site, but this strategy can only be used when the appropriate staging and transportation conditions existing. Usually, precasting in bridge bents is limited to the columns and beams. To facilitate fabrication, transportation and erection convenience, the connections are usually made at the top and bottoms of the columns. This strategy facilititates construction, but it can be challenging in seismically hazardous areas, because the ends of columns have high seismic demands.

Haraldsson et al. (2013) described the development of a "socket" connection between a precast column and cast-in-place footing. This chapter describes the concept, and seismic performance of the connection between a precast column and drilled shaft, and provides recommendations to ensure desirable performance.

2.2 CONCEPT

The “wet” socket connection concept was proposed by Haraldsson et al. (2013) to connect a precast column with a cast-in-place spread footing. In that connection, the bottom of the precast column is roughened where it will be embedded in the cast-in-place spread footing. The ends of the longitudinal column reinforcement is terminated with mechanical anchors instead of using the more conventional detail of bending the longitudinal bars outwards into the foundation.

Deep foundations are often needed in many soft-soil conditions, so in this research, the socket concept has been adapted to connections between a precast column and cast-in-place drilled shaft. The construction sequence is shown in Figure 2.1. Construction SequenceOnce the shaft has been excavated, the shaft reinforcing cage is placed, and concrete is cast until reach the bottom level of the transition (Step 1). The precast column is then positioned and braced (Step 2), and the transition is cast (Step 3). Finally, the cap beam is constructed to connect with the columns (Step 4).

In this new connection, the precast column is intentionally roughened (as was done by Haraldsson et al. 2013) where it is embedded in the cast-in-placed enlarged drilled shaft. The transition region needs to be strong enough to develop the flexural strength of column. To make the transition region as short as possible, mechanical anchors are used for column bars to reduce the development length of longitudinal reinforcement in the transition region (Fig. 2.2).

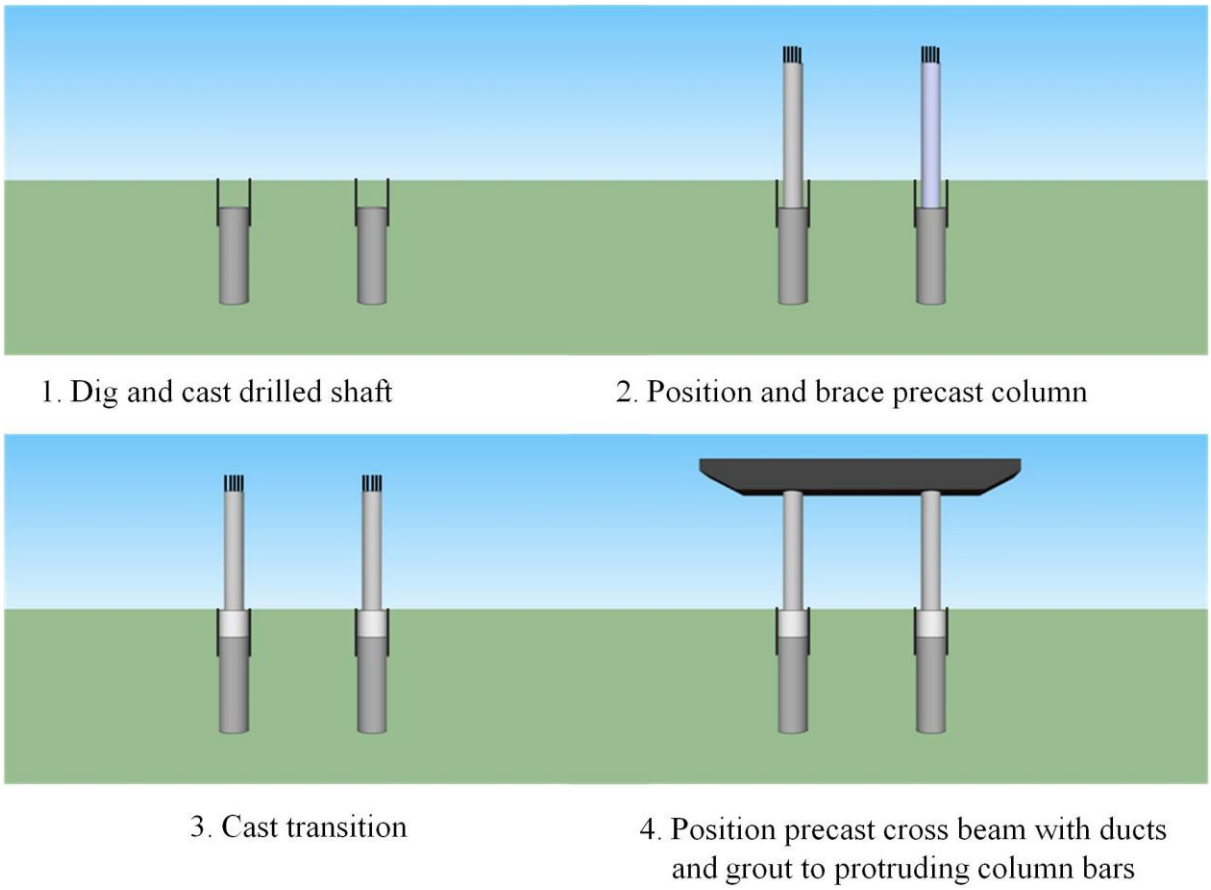

Figure 2.1. Construction Sequence

2.3 QUASI-STATIC TESTS

Three column-drilled shaft connection specimens (DS-1, DS-2, and DS-3) were tested at the University of Washington to evaluate the seismic performance of the connection, and to provide data with which to calibrate a design methodology. The test specimens were designed according to the AASHTO Load Resistant Factor Design 2009, AASHTO Guide Specifications for LRFD Seismic Design 2009, and WSDOT Bridge Design Manual (2012) with the exception of the spirals in the transition region.

2.4 SPECIMENS

The test specimens key dimensions and reinforcement are shown in Table 2.1. The only difference between Specimen DS-1 and Specimen DS-2 was that the amount of spiral in the column-to-shaft transition region was reduced by half in DS-2. The test specimen dimension and reinforcement in Specimen DS-1 and DS-2 were scaled (1/3.6) from a real prototype, and Specimen DS-3 had more column and shaft reinforcement, but with a smaller shaft diameter.

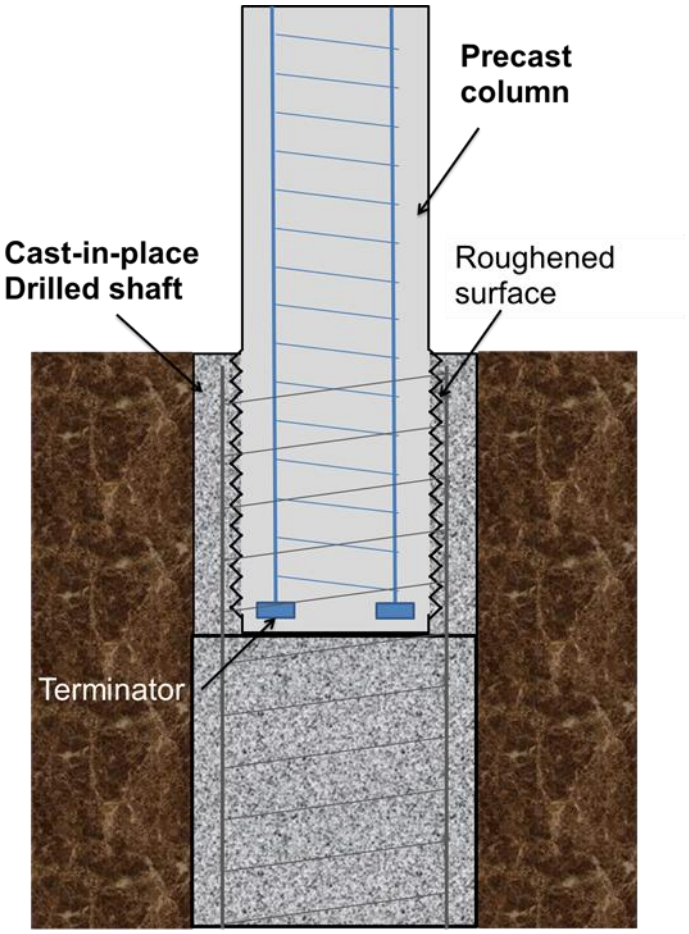

Figure 2.2. Column-to-Shaft Connection Concept

The embedded length of the column in the drilled shaft (28 in.) was based on the scaled-down non-contact lap splice length of the shaft prototype according to WSDOT BDM (proposed by McLean et al. (1997)), given as

$$l_{ns} = l_s + e$$

where:

l_{ns} = length of noncontact lap splice.

l_s = lap splice length required by AASHTO LRFD 5.11.5.3 or

$l_s = 1.7 l_d$ (for a Class C lap splice) where l_d is the longer development length of either column or shaft bars. In our case, mechanical anchors were used only for column bars, so the development length is controlled by shaft bars.

$e =$ distance between the shaft and column longitudinal reinforcement.

The shaft longitudinal reinforcement was designed to form a plastic hinge in the column. Therefore, the yield moment of the shaft had to be larger than the moment at the base of the shaft due to the over-strength moment and shear from the column above.

The shaft spirals were designed based on the non-contact lap splices behavior, but using different value of efficiency factor. McLean et al. (1997) proposed a formula to determine spiral spacing as:

$$s_{tr} = \frac{2\pi A_{sp} f_{ytr} l_s}{A_l f_{ul}}$$

where,

A_{tr} = area of shaft transverse reinforcement or spiral (in.^{2})

A_l = total area of longitudinal column reinforcement (in.^{2})

f_{yt} = specified minimum yield strength of shaft transverse reinforcement (ksi)

f_{ul} = specified minimum tensile strength of column longitudinal reinforcement (ksi), 90 ksi for A615 and 80 ksi for A706

l_s = Class C tension lap splice length of the column longitudinal reinforcement (in.)

s_{tr} = spacing of shaft transverse reinforcement (in.)

WSDOT BDM adjusts this formula by adding to the divisor a factor, k, representing the ratio of column tensile reinforcement to total column reinforcement at the nominal resistance. This factor is to be determined from column moment-curvature analysis or, as a default, taken as k = 0.5. In

our case, the shaft spirals were designed with three different value of factor k = 0.5, 0.25, and 1.0 in Specimen DS-1, DS-2, and DS-3 respectively.

Table 2.1. Specimens Configuration

	DS-1	DS-2	DS-3
Column Diameter	20 in.	20 in.	20 in.
Clear Column Height	60 in.	60 in.	60 in.
Column Longitudinal Reinforcement Ratio	1.0 % (10#5)	1.0 % (10#5)	1.6 % (16#5)
Column Transverse Reinforcement	0.8 % (gage-3 @ 1.25 in. pitch)	0.8 % (gage-3 @ 1.25 in. pitch)	0.8 % (gage-3 @ 1.25 in. pitch)
Shaft Diameter	30 in.	30 in.	26 in.
Shaft Height	30 in.	30 in.	30 in.
Transition Length	28 in.	28 in.	28 in.
Shaft Longitudinal Reinforcement Ratio	0.9 % (30 bundles of 2#3)	0.9 % (30 bundles of 2#3)	2.7 % (24 bundles of 3#4)
Shaft Transverse Reinforcement	0.14 % (bundle of 2 gage-9 @ 3.0 in. pitch)	0.07 % (1 gage-9 @ 3.0 in. pitch)	0.40 % (bundle of 3 gage-9 @ 1.5 in. pitch)
Lateral Reinforcement Efficiency Factor [k]	0.50	0.25	1.00

WSDOT BDM requires three turns of wire at the end to terminate the spiral. Thus, 6, 3, and 9 turns of spiral were placed at the top of the transition in Specimen DS-1, DS-2, and DS-3 respectively.

The bottom of the shaft connected with a cast-in-place footing to attach the specimen to the testing rig. The longitudinal bars of the drilled shaft were hooked at the bottom mat of footing.

2.5 TEST PROTOCOL

The specimens were placed in a self-reacting rig as shown in Fig. 2.3. First, an axial load of 159k was applied in the column to represent the un-factored dead load. This axial load was kept constant until the end of testing. Later, the specimen was subjected to horizontal displacement. The displacement history was the same as in previous test by Pang et al. (2008), Haraldsson et al. (2011), and Janes et al. (2011). This displacement history was a modification of a loading history for precast structural walls recommended in NEHRP (Building Seismic Safety Council). The testing stopped when nearly all of the column bars or shaft spirals fractured.

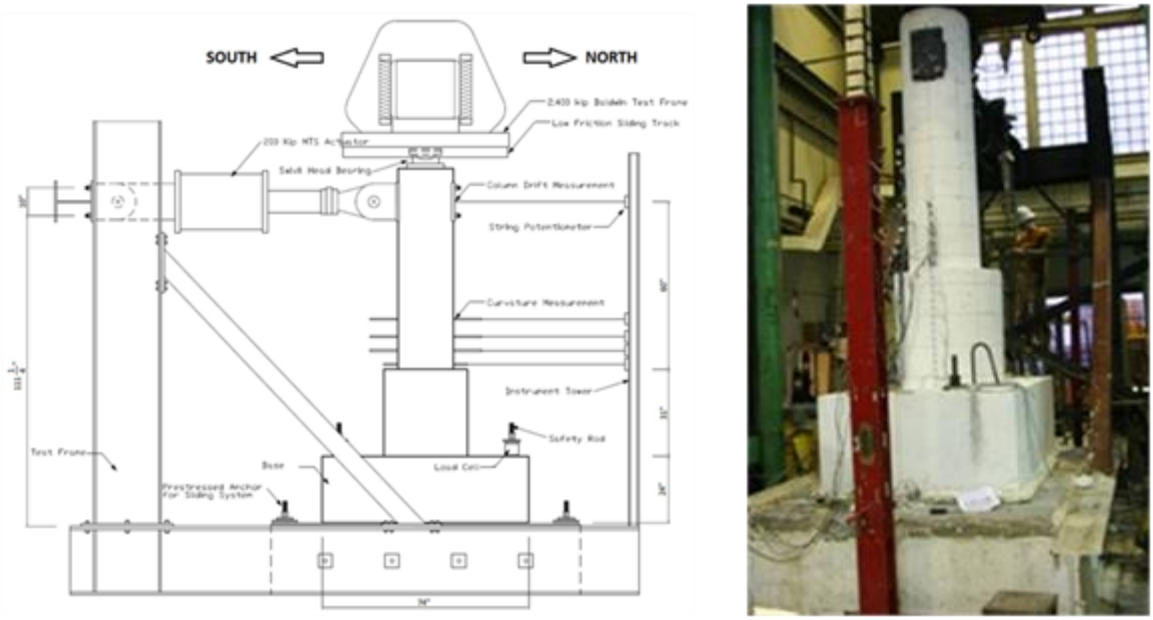

Figure 2.3. Test Setup

2.6 SUB-ASSEMBLY RESPONSE

Fig. 2.4 shows the moment vs. drift ratio response of the test specimens DS-1, DS-2, and DS-3. Under cyclic loading, in both specimens DS-1 and DS-3, failure occurred by plastic hinging in the column while the connection region in the foundation remained generally undamaged. However, in Specimen DS-2, failure occurred in the connection region after some cracks had first occurred in the column, as shown in Fig. 2.5.

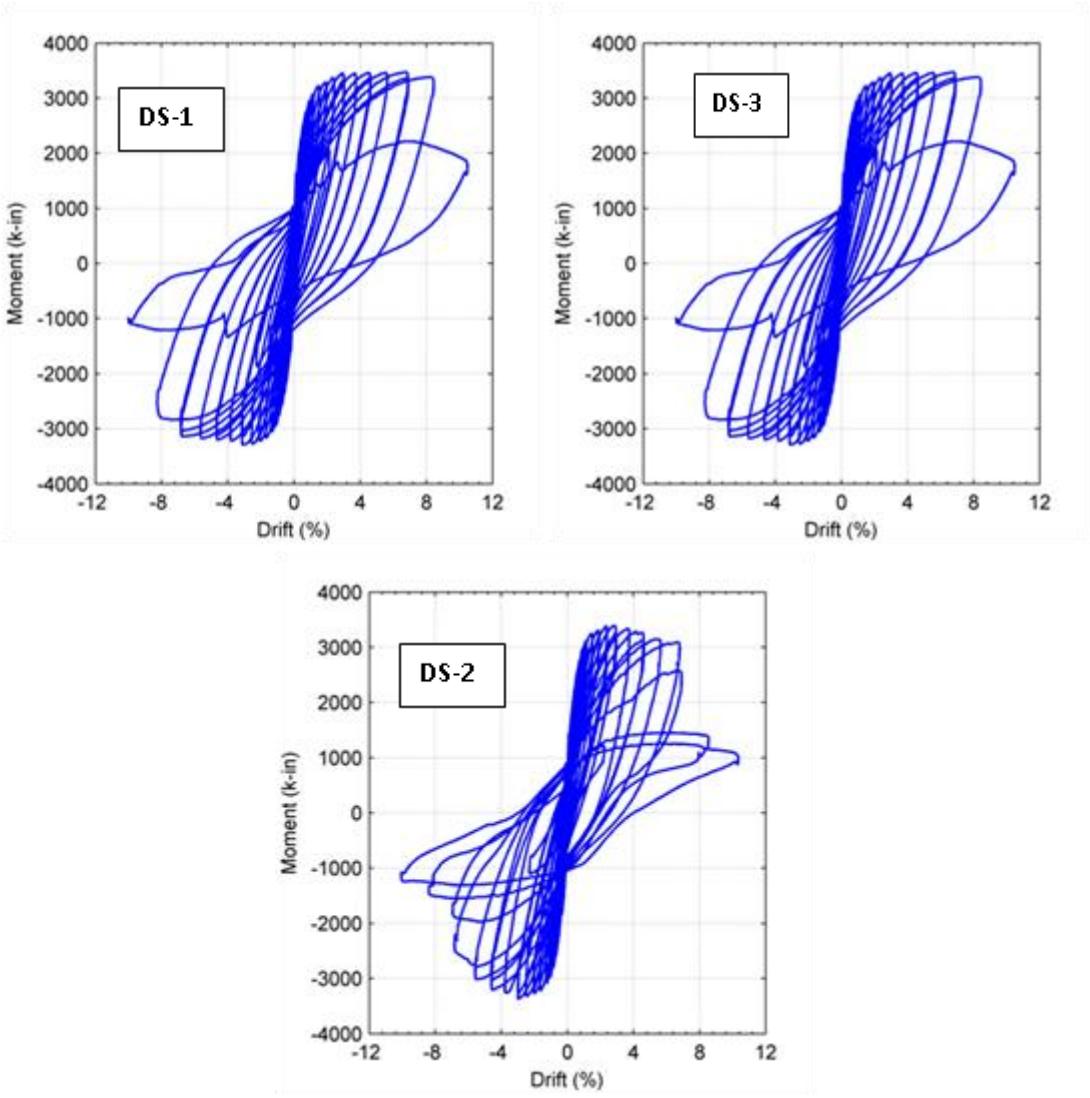

Figure 2.4. Moment-Drift Ratio Response

In all cases, the yield moment occurred at about 1.5%-2.0% drift ratio. The moment capacity dropped below 80% of the peak value at 7%-8% drift ratio. The responses of Specimens DS-1 and DS-3 were very ductile. The similarity between the peak strengths in specimens DS-1 was expected because the column were nominally identical previous column-to-spread footing tests (Haraldsson et al. (2011)) and the specimen strength was controlled by the column response.

Under cyclic loading, the strain gauge attached in the shaft spirals in all three specimens showed that the horizontal strain distributions in the transition spirals were not uniform. The horizontal strains were largest in the upper part of the transition, and almost zero at the bottom of the transition during cyclic testing. In specimens DS-1 and DS-3, the horizontal strains at the top of the transition passed the yielding point. All shaft spirals fractured in Specimen DS-2 after testing. The specimens response proved that the three turn of spirals at the top of the transition, which is not considered in designing, had a great contribution to the horozontal resistance of the connection.

For each of the specimens, the damage to the connection after testing ais shown in Fig. 2.5. In Specimens DS-1 and DS-3, plastic hinges formed in the column and the mode of failure were column failure as desired. The shaft just had some cracking and damage of the concrete cover at the top of the shaft, but almost strains measured in longitudinal and transverse reinforcement were smaller than yielding point.

However, the plastic hinge did not form in the column in Specimen DS-2. No obvious concrete spalling occured in the column during the cyclic test. The system was damaged by prying failure happened in the shaft. The strain measured in the longitudinal reinforcement proved that there was no bonding failure during testing as predicted in designing.

a) DS-1

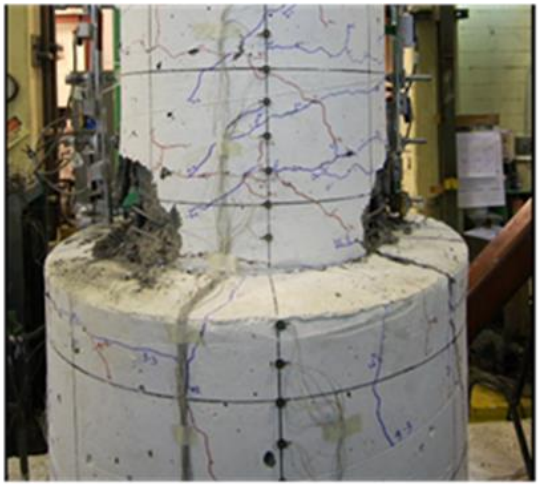

b) DS-2

c) DS-3

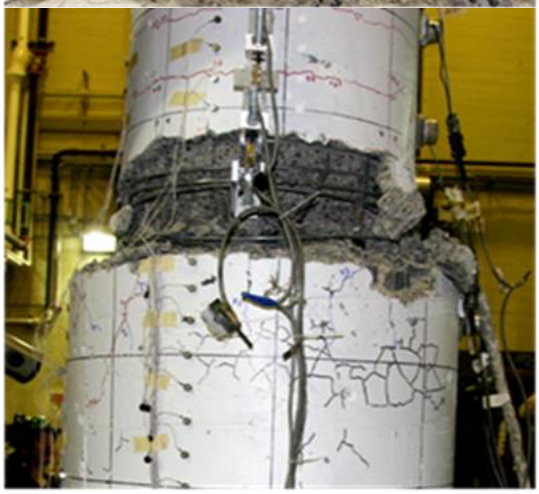

Figure 2.5. Specimen Damage After Testing

2.7 CONCLUSIONS FROM TESTING

A new type of connection between a precast concrete column and a oversize drilled shaft using “wet” socket connection has been developed. This connection system has many advantage of rapid construction, and performes well in high seismic regions.

From the results obtained in three tests performed in the University of Washington, the following conclusions and recommendations can be drawn:

- The proposed amount of confinement reinforcement required for the column-to-shaft connection protects the shaft and causes failure to occur by plastic hinging of the precast column, as desired. The test specimens had the smallest possible shaft/column diameter ratio, and the shortest possible embedment length, so this conclusion can hold for all permissible shaft and column combinations.
- The confinement reinforcement of the shaft should satisfy the WSDOT equation mentioned above. However, the factor ***k*** should be used as an efficiency factor instead of a factor representing the ratio of column tensile reinforcement to total column reinforcement.
- The three turns of spiral at the top of the transition region, which is not calculate in design equation, provides extra resistance. They were the first fractured spiral turn in Specimen DS-2, and yielded in both Specimen DS-1 and DS-3. These amount of spiral are equivalent as the efficiency factor k = 1.5, 0.75, and 1.5 in Specimens DS-1, DS-2, and DS-3 respectively. Therefore, it suggests that the spirals at the top of the transition region should be designed with a efficiency factor $k > 1.5$
- The horizontal strain distributions in the transition region is largest at the top and almost zero at the bottom of the transition. Therefore, it will be more efficient if more

spirals are placed in the upper part and less spirals are placed in the lower part. The spiral strain at the middle of the transition length was nearly yielding in Specimen DS-1 (designed with k = 0.5), but was equal as about 50% of yielding strain in Specimen DS-3 (designed with k = 1.0). Thus, it suggests that the spirals should be designed with a efficiency factor k = 1.0 for the upper part, and k = 0.5 for the lower part of the transition to ensure that all spiral will be in elastic region.

- Prying failure of the concrete shell surrounding the precast column will occur if inadequate confinement reinforcement is provided.
- If the external steel tube were used, it might provide some of the benefits of additional spiral, and force the failure back into the column.
- Mechanical anchor heads are needed at the ends of the column longitudinal reinforcement to ensure hinging in the column without anchorage failure, especially if the large bar system

CHAPTER 3

STRUT-AND-TIE MODEL FOR CONNECTIONS BETWEEN PRECAST CONCRETE COLUMNS AND DRILLED SHAFTS

3.1 INTRODUCTION

In this chapter a strut-and-tie model is developed to proportion the transverse reinforcement for the transition region between the column and the drilled shaft.

First, the forces acting at the connection boundaries for the seismic loading are estimated (Section 3.2). This estimate is done using sectional analysis of the elements that adjoin the transition region, namely the column and the shaft. These sectional analyses allow the designer to identify the longitudinal force resultants and their locations within the cross-sections.

Next, a strut-and-tie model of the transition region is developed to resist the forces from the sectional analyses acting at the boundaries (Section 3.3). The elements of the strut-and-tie model transfer the forces internally between their points of application on the boundary. The computed forces in model elements are evaluated by comparing them with values derived from the experiments (Section 3.4), and the lateral capacity of the system is evaluated in terms of the capacities of the struts and ties.

3.2 FORCES ACTING ON THE BOUNDARY OF THE TRANSITION REGION

To use a strut-and-tie model, it is necessary to estimate the force resultants and their locations at the model boundaries. These forces are shown schematically in Figure 3.1.

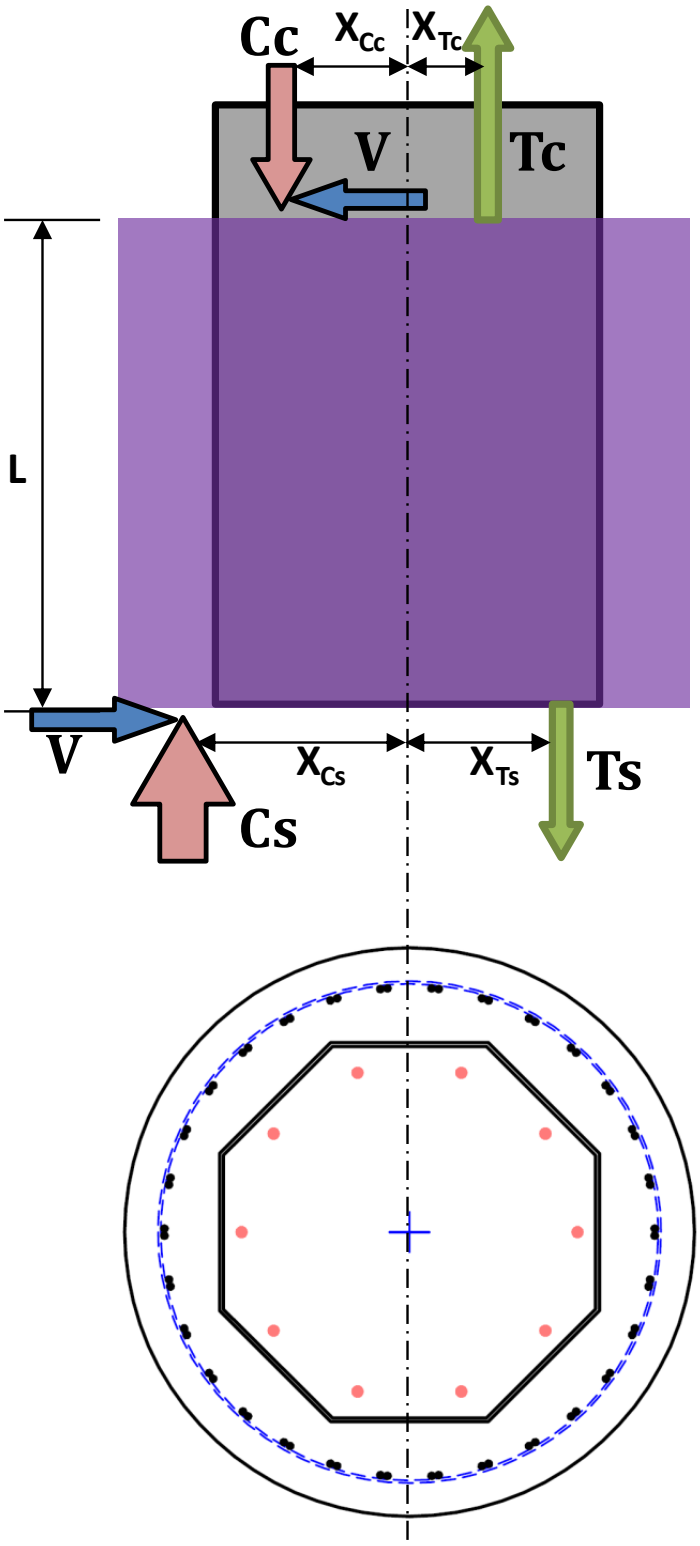

Figure 3.1. Forces Acting at the Boundary of the Column-Shaft Connection.

To determine the appropriate values of the flexural tension and compression resultant forces, and their locations forces at the boundaries of the transition regions, moment-curvature analyses were performed for both the column and shaft cross-sections. At high drift ratios, a plastic hinge may form at the bottom of the column, if some other element has not failed before. Hung (2015) found that the moments and the steel strains predicted by the cross-sectional analysis were close to those measured in the laboratory tests, so they were judged to be sufficiently accurate to predict the forces at the boundaries of the strut-and-tie model.

For example, the calculated moment-curvature relationships for the columns are shown in Figure 3.2. The flexural strengths predicted by the analyses and measured values are listed in Table 3.1. For specimens DS-1 and DS-2 the moments predicted by both analyses give values within 2-4% of the measured peak moment. These results suggest that the differences in the longitudinal reinforcement properties did not greatly affect the flexural strength of the column. Both analyses resulted in the ultimate flexural strength occurring at a curvature of 0.0065 rad/in.

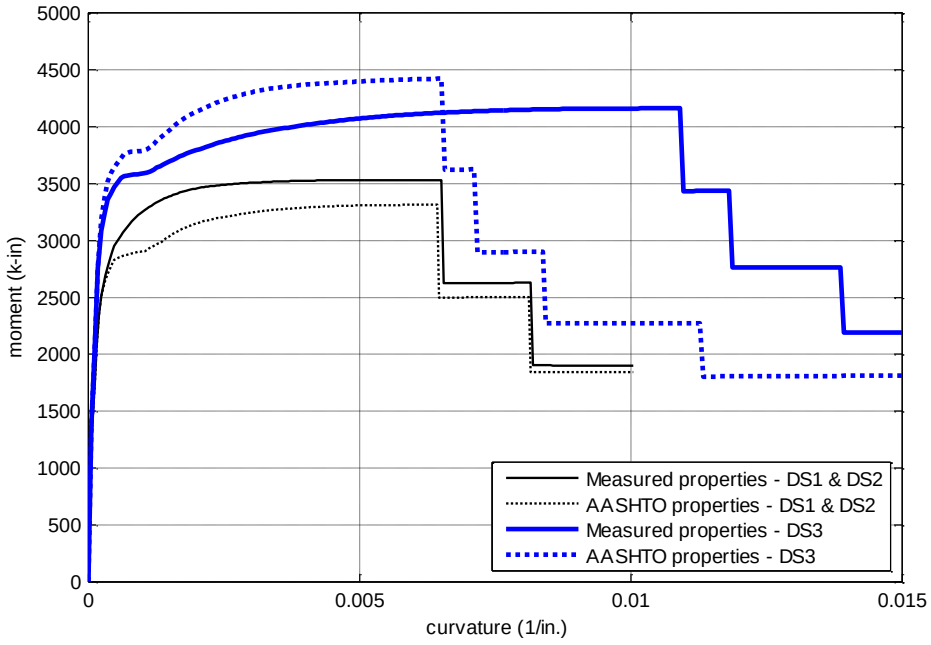

Figure 3.2. Moment-Curvature Analyses of Columns

Table 3.1. Comparison of Peak Column Moments

Specimen	Moment calculated using expected properties [kip-in.]	Moment calculated using measured properties [kip-in.]	Measured moment [kip-in.]	Ratio of measured to predicted moment using measured properties
DS1	3315	3530	3476	0.98
DS2	3315	3530	3393	0.96
DS3	4423	4165	3622	0.87

3.3 STRUT-AND TIE MODEL FORMULATION

In the previous section, it was shown that sectional analysis can be used to establish the forces and their locations acting at the boundary of the column-shaft connection. At a given curvature and moment, the predicted values agree with the measured ones. In this section, transfer of these forces through the transition region is investigated. A strut-and-tie model is proposed and compared with measured data in the next section.

3.3.1 Free-Body Diagram Before Failure

As discussed in Chapter 5, Specimen DS-2 failed in the transition region. The damage levels for Specimen DS-2 just before and after the measured lateral load resistance decreased below 80% of the maximum resistance obtained earlier in the test is shown in Figure 3.3. The behavior of this specimen was characterized by the opening of large vertical and diagonal cracks in the transition, and followed subsequently by fracture of the spirals.

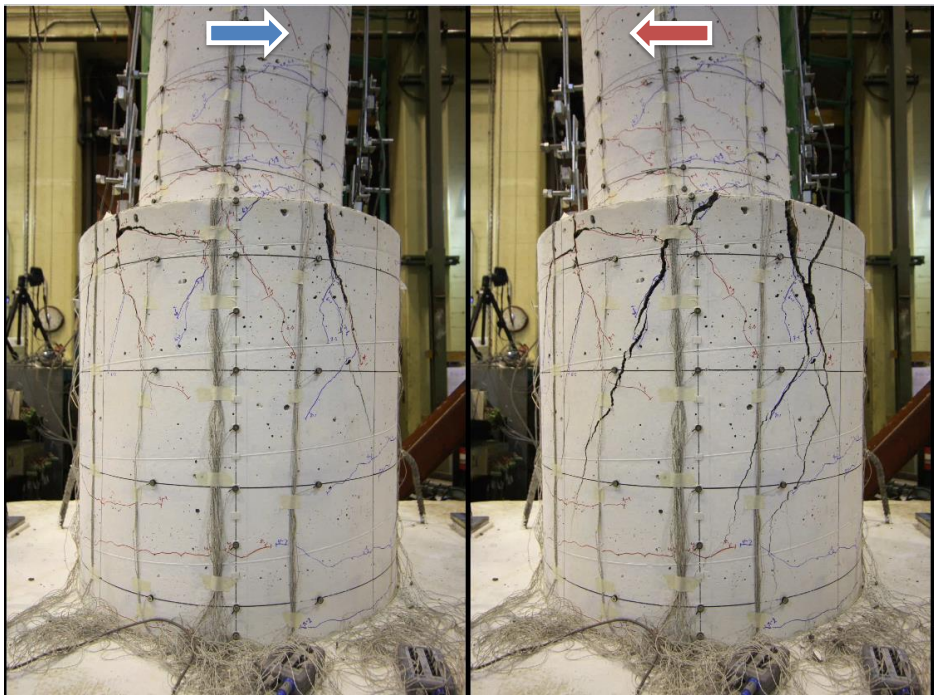

a). Cycle 9-2 Peak - drift +6.8 % b). Cycle 9-2 Valley - drift -6.8 %

Figure 3.3. Specimen DS-2: Before and After Failure

The free-body diagram of the left-hand part of Specimen DS-2 before failure gives an interpretation of the behavior and failure mode of the column-shaft connection. Based on the prying failure of Specimen DS-2 (Figure 3.3b), the free body diagram of the left part of the transition is demonstrated in Figure 3.4.

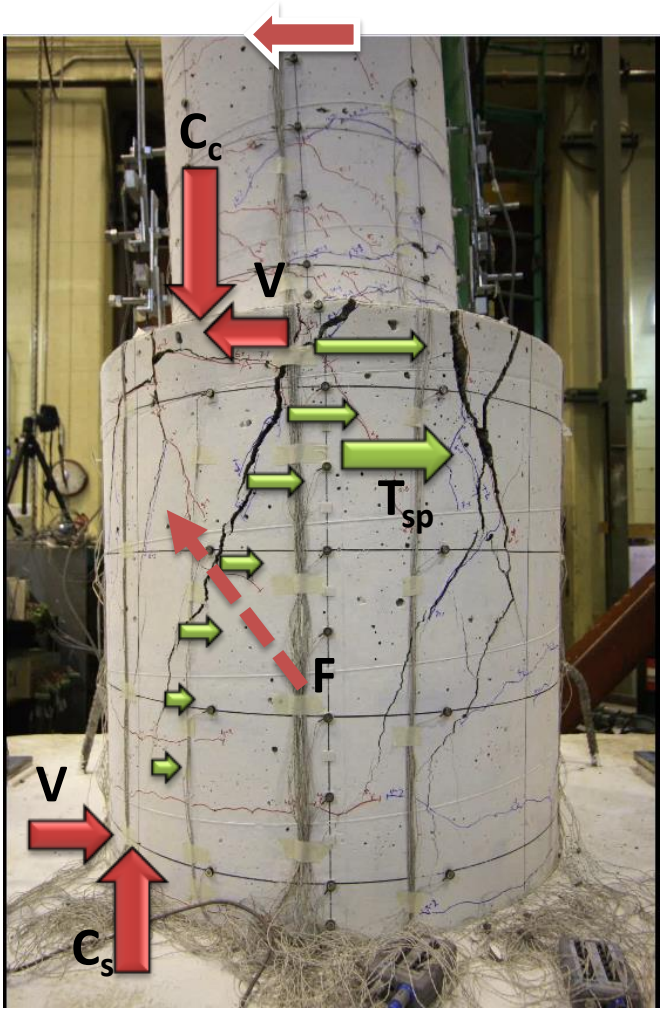

Figure 3.4. Free-Body Diagram – DS-2

As shown in the free body diagram, the applied forces include compressive resultant force of column and shaft ($\boldsymbol{C_c}$ and $\boldsymbol{C_s}$ respectively), shear forces, $\boldsymbol{V}$, at the top and bottom, and spirals tensile forces (marked as green arrow) distributed along diagonal cracks with resultant at $\boldsymbol{T_{sp}}$. The diagonal face includes both column and shaft part. The spirals tensile force was acting at the shaft part .Because the column diameter was smaller than shaft diameter, normally, $\boldsymbol{C_c}$ was larger than $\boldsymbol{C_s}$. For equilibrium, force $\boldsymbol{F}$, which has vertical part is equal to $\boldsymbol{C_c - C_s}$ and horizontal part is equal to $\boldsymbol{T_{sp}}$,is needed at the column part of the diagonal face.

3.3.2 Strut-and-Tie Model

Based on the forces acting at the boundary region and free-body diagram, the force transferred from the column to the shaft is represented by a proposed strut-and-tie model as shown in Figure 3.5.

The boundary conditions for the strut-and-tie model were determined as follows:

- The column tension force $\boldsymbol{Tc}$ was represented by a tie element. The location ($\boldsymbol{X_{Tc}}$) and magnitude of this tie was equal to the column tensile resultant force's location and magnitude that were estimated from the moment-curvature analysis of the column section.
- Similarly, the locations of nodes **E** and **F** were identified at the calculated locations of the column and shaft compression resultant force respectively using moment and force equilibrium requirement.
- The shaft tension force $\boldsymbol{Ts}$ was represented by a tie element, which is located ($\boldsymbol{X_{Ts}}$) at the shaft tensile resultant force estimated from the moment-curvature analysis of the shaft section.

The internal elements of the model were determined as follows:

- The elevation of node **A** was assumed to be at the end of column headed bars.
- The transition transverse reinforcement was represented by tie **BC**. This tie was placed horizontally at the location of the transition transverse resultant force. In the analysis model, this location is determined based on the strain data attached on the transverse reinforcement. In the design model, it is determined based on the assumed parabolic strain distribution of the transverse reinforcement assumption which will be discussed more in the design model section.

- Struts **CE** and **DF** were identified based on equilibrium considerations of nodes **E** and **F**.
- Node **B** and **C** were placed at the intersection between tie **BC** and **Ts**, **EC** respectively
- Strut **AB** represented the lap splice force transfer mechanism between column and shaft reinforcement. This strut is not a real strut in the transition region. It was the resultant force of all compressive struts transferred from column to shaft reinforcement which were uniformly distributed inside the peripheral hoops or spirals. Strut **AB** was also needed to maintain equilibrium at nodes **A** and **B**.
- To maintain equilibrium at node **A**, strut **AD** was established.
- Node **D** was placed at the intersection between struts **DF** and **AD**.
- Strut **CD** was located to maintain equilibrium at nodes **C** and **D**.

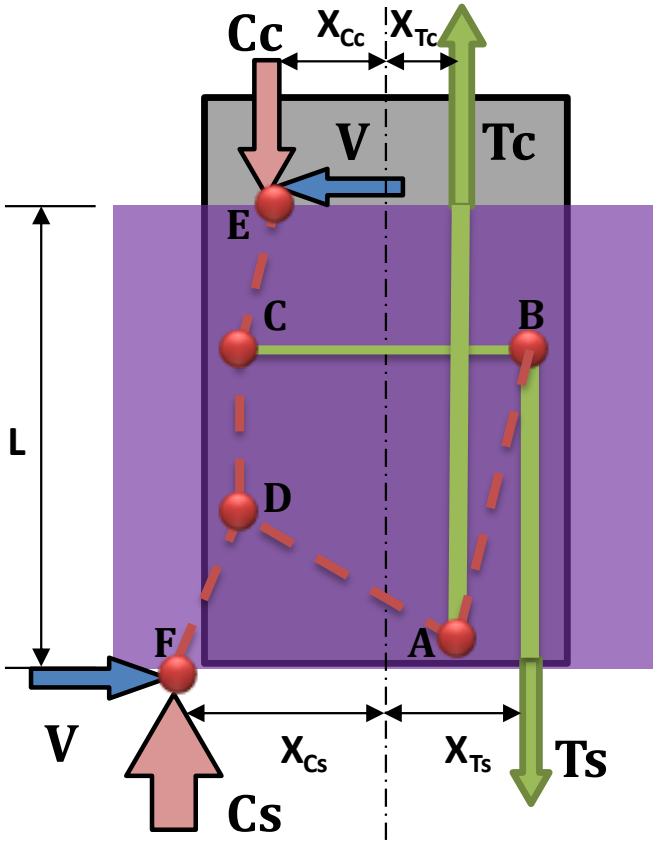

Figure 3.5. Proposed Strut-and-Tie Model.

3.4 VERIFICATION OF STRUT-AND TIE MODEL

The key transition failure modes and the lateral-load capacity of the system are evaluated in terms of the capacities of the proposed struts and ties in this section. Hung (2015) provides more details about the calculated and measured capacities.

3.4.1 Compression Failure

The system investigated here is the connection between a column and an enlarged shaft. Thus, the compressive stress in the column is larger than in the shaft. Therefore, in general, the compression failure will not happen in the transition.

3.4.2 Tension Failure

A tension failure is developed in the column when the hinge forms in the column and the column longitudinal reinforcement is subjected to large inelastic strain. This is the desired mode of failure of the column-shaft connection. In the strut-and-tie model, this mode of failure is represented when the column tensile resultant force **Tc** is more than the tensile resultant force estimated from the moment-curvature analysis.

3.4.3 Anchorage Failure

In order to obtain a satisfactory performance of the column-shaft connection, it is essential that the column longitudinal reinforcement is sufficiently anchored into the transition. If an anchorage failure of column reinforcement occurs, a tensile failure cannot and the desired response mode of a column flexural above the shaft cannot be achieved. Since it is desirable to form a plastic hinge in the column and the shaft reinforcement remains elastic, high inelastic strains with opposite sign are typically developed in the column reinforcing bars. In the

investigated column-shaft connection, the ends of the longitudinal column reinforcement were terminated with rebar end anchors. Thus, the anchorage failure is not likely to happen.

3.4.4 Lap Splice Failure

The lap splice failure occurs if the confining pressure is not sufficient to prevent splitting of concrete between the column and shaft longitudinal reinforcement, so the column tension force may not be transferred to the shaft reinforcement by bond or shear friction across the precast-c.i.p interface. Thus, the transition will fail before the column reaches its flexural strength. Specimen DS-2 was designed with a small amount of transition spiral, which was expected to induce lap splice failure. However, the test result showed that even when some of the spirals were broken, the tension force in the shaft reinforcement did not change (Figure 3.6). It suggests that the splice failure can be prevented by a minimum requirement of transverse reinforcement.

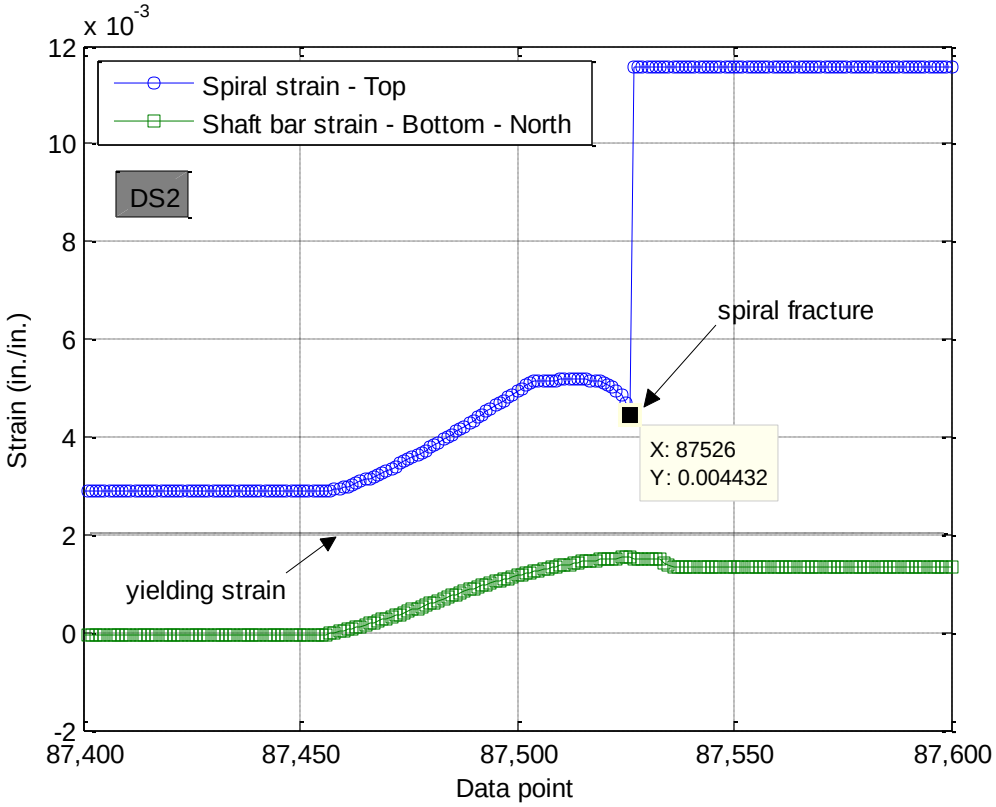

Figure 3.6. Spiral Fracture Point (Specimen DS-2)

3.4.5 Prying Failure

The prying failure occurs if the transverse reinforcement is not sufficient as shown in Specimen DS-2 (Figure 3.3b). In contrast with the lap splice failure, the prying failure occurs even when the tension force still can transferred from column to shaft reinforcement. This is because only the spirals at the top part of the transition were activated in the prying behavior. When the top spirals were broken, the lower spirals were activated. This mode of failure is similar to the zip behavior as the two rows of teeth are separated if the slider moves down. Therefore, if the transverse reinforcement is uniformly distributed in the transition, the prying failure still can happen. This mode of failure is represented in the proposed strut-and-tie model when the force in tie element **BC** exceeds its strength.

3.4.6 Verification of Proposed Strut-and-Tie Model

As shown above, the compression failure, anchorage failure, and lap splice failure did not occur in the three test specimens. The tension failure (or flexural failure) happened in specimens DS-1 and DS-3 and prying failure happened in Specimen DS-2. The criterion used to evaluate the proposed strut-and-tie model was the magnitude of tie force BC agree with the resultant force of spirals in the test results of the three specimens.

First, the tensile force in the spirals were calculated based on strain calculated by using the horizontal displacement of the shaft as follows:

- Under cyclic excitation, the shape of the shaft deformation was assumed as an ellipse shape as shown in Figure 3.7. Assuming that the semi-minor axis, **b**, is equal to the radius of the shaft spiral, **R**. The semi-major axis, **a**, is measured as a half of the distance between the North and South LED marker of Optotrak.
- The perimeter of the ellipse is calculated using Ramanujan's formula as follows:

$$p \approx \pi \left[3(a+b) - \sqrt{(3a+b)(a+3b)}\right] \tag{6-1}$$

- The average strain of spiral is calculated as:

$$\epsilon_{sp} = \frac{\Delta L}{L} = \frac{p - 2\pi R}{2\pi R} \tag{6-2}$$

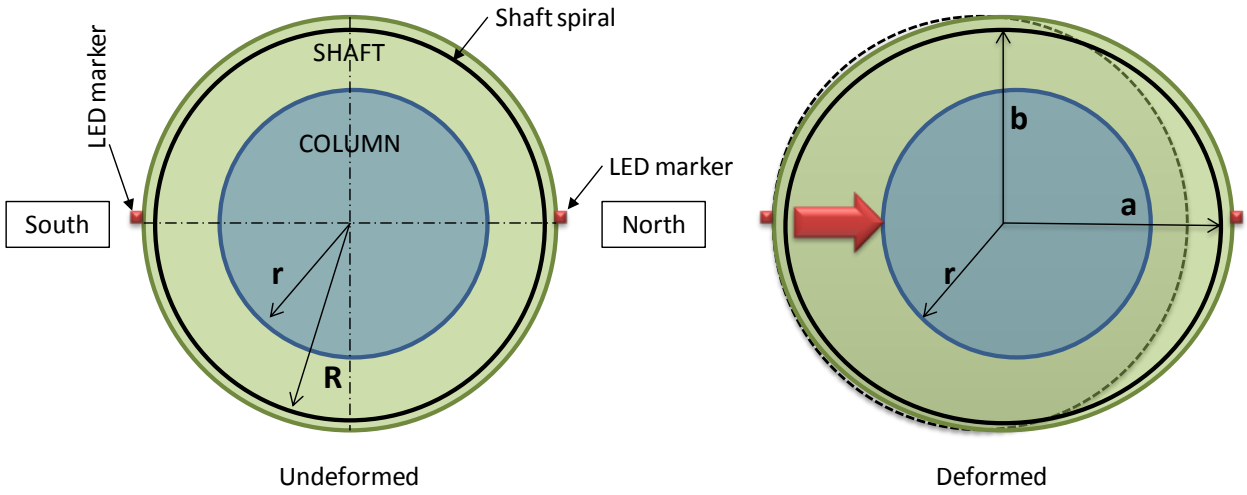

Figure 3.7. Section of Column-Shaft Connection Before and After Deformation

The comparison of spiral strain measured by the above method and the strains measured by electrical strain gauges at some points are shown in Figure 3.8 and Figure 3.9 for specimens DS-1 and DS-2. In those figures, the "calculated strain" refers to the strains calculated with the motion capture system (Optotrak) deformation data. It indicates that the strains measured by the above method are in good agreement with the strain gauge data.

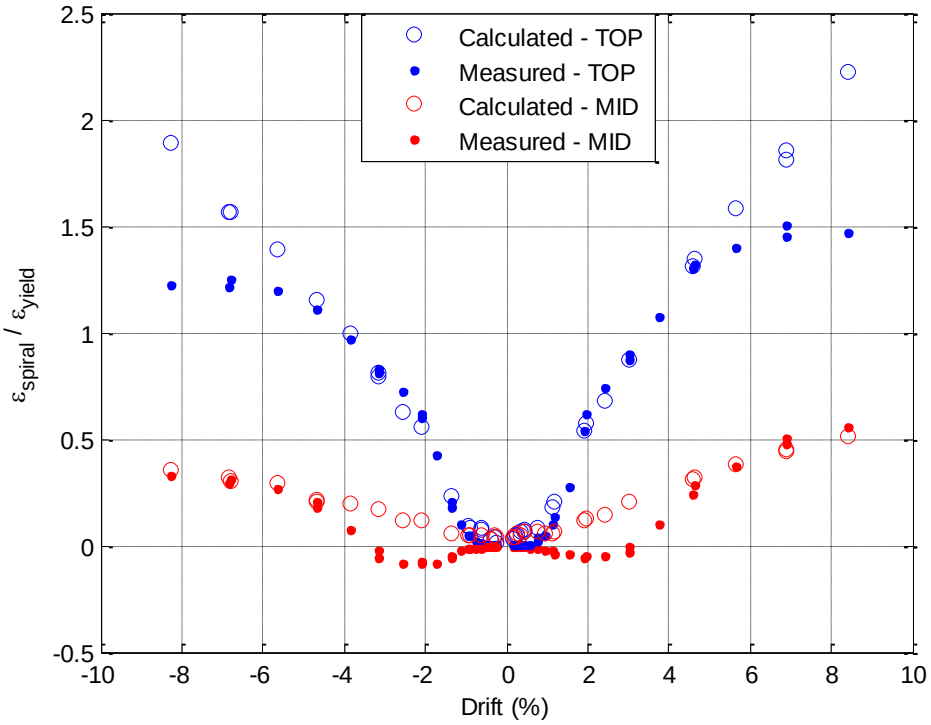

Figure 3.8. Comparison of Calculated and Measured Spiral Strains – DS-1

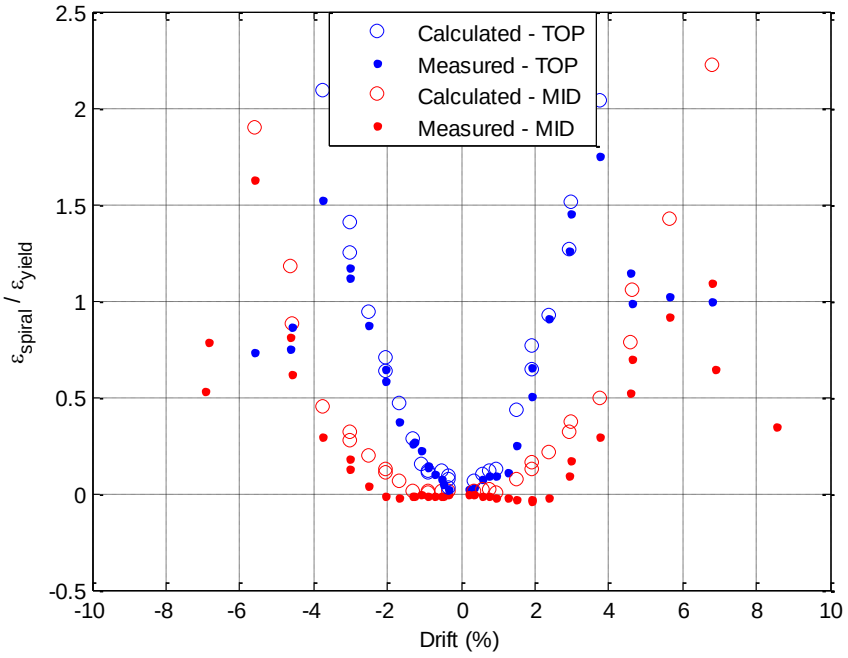

Figure 3.9. Comparison of Calculated and Measured Spiral Strain – DS-2

The stresses and tensile force of shaft spirals were calculated using the stress-strain relationship which measured in a tension test. The values of spiral force, which were calculated using strain calculated from the Optotrak data are assumed to be the measured value, since they gave a better strain distribution along the connection in comparison with using strain gauge data.

The comparison of the measured and calculated value of the spiral resultant force **Tsp** using the proposed strut-and-tie model were shown in Figure 3.10 and Figure 3.11 for specimens DS-1 and DS-2. The difference between the measured and calculated **Tsp** in specimens DS-1 and DS-2 represents the contribution of shaft concrete tensile strength. In Specimen DS-3, when the shaft diameter was reduced, the calculated values were close to the measured values.

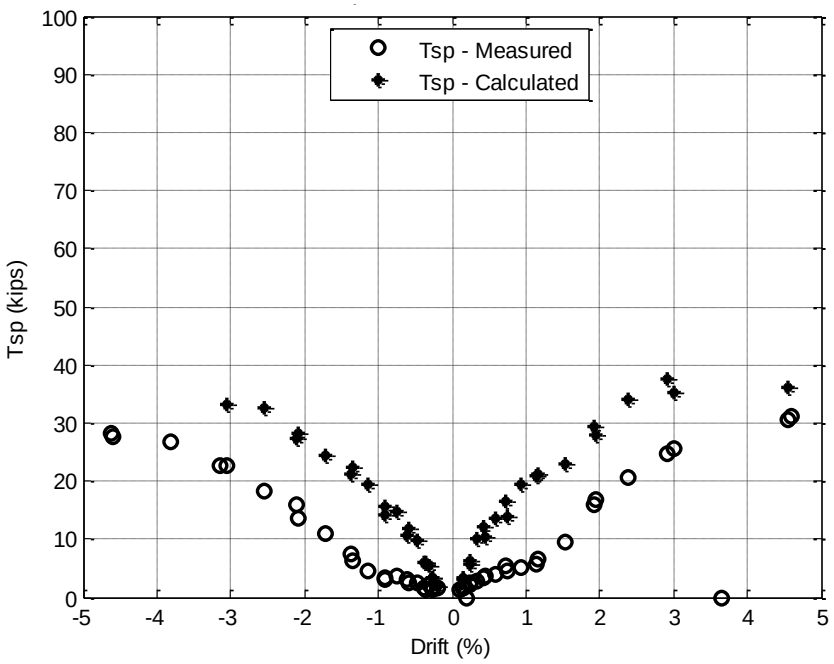

Figure 3.10. Spiral Resultant Force vs. Drift – DS-1

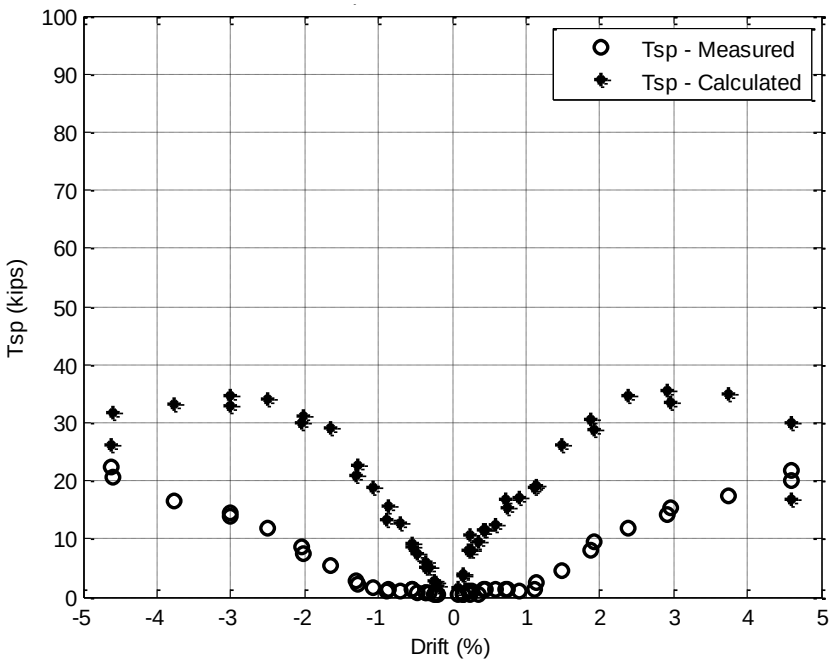

Figure 3.11. Spiral Resultant Force vs. Drift – DS-2

Specimens DS-1 and DS-3 failed because of column bars fracture after a hinge formed in the column and the column moment strength reduced dramatically. Specimen DS-2 failed because the top shaft spirals fractured before a hinge formed in the column. Therefore, to determine the mode of failure of the column-shaft connection, the ratio of column moment to column ultimate moment (i.e. moment strength which is the maximum moment measured in specimen DS-1 and DS-3. In Specimen DS-2, moment strength is taken the same as in Specimen DS-1 since they have the same design and material) $\boldsymbol{M_c/M_{c,ult}}$ should be compared with the ratio of spiral resultant force to spiral ultimate force $\boldsymbol{T_{sp}/T_{sp,ult}}$. If the ratio $\boldsymbol{M_c/M_{c,ult}}$ reaches 1 first, the system fails in column. In contrast, if the ratio $\boldsymbol{T_{sp}/T_{sp,ult}}$ reaches 1 first, the system fails in the transition. Since it is desirable to form a plastic hinge in the column when the shaft reinforcement remains elastic, the ratio $\boldsymbol{T_{sp}/T_{sp,ult}}$ is replaced by the ratio $\boldsymbol{T_{sp}/T_{sp,yield}}$ where, $\boldsymbol{T_{sp,yield}}$ is the spiral resultant force when the strain of the top spiral turn reaches yielding strain.

The relationship between ratio $\boldsymbol{M_c/M_{c,ult}}$ and ratio $\boldsymbol{T_{sp}/T_{sp,yield}}$ for both measured and calculated values are shown in Figure 3.12, Figure 3-13, Figure 3-14 for specimens DS-1 and DS-2, and DS-3 respectively. It indicates that the predicted values of strut-and-tie model were in good agreement with the measured values, and it could determine the mode of failure of all tests. However, it also can be seen that even the hinge formed in the column in specimens DS-1 and DS-3, the ratio $\boldsymbol{T_{sp}/T_{sp,yield}}$ also more than 1. It suggests that the amount of spiral designed for these tests were still not enough to keep the transition spirals remain elastic.

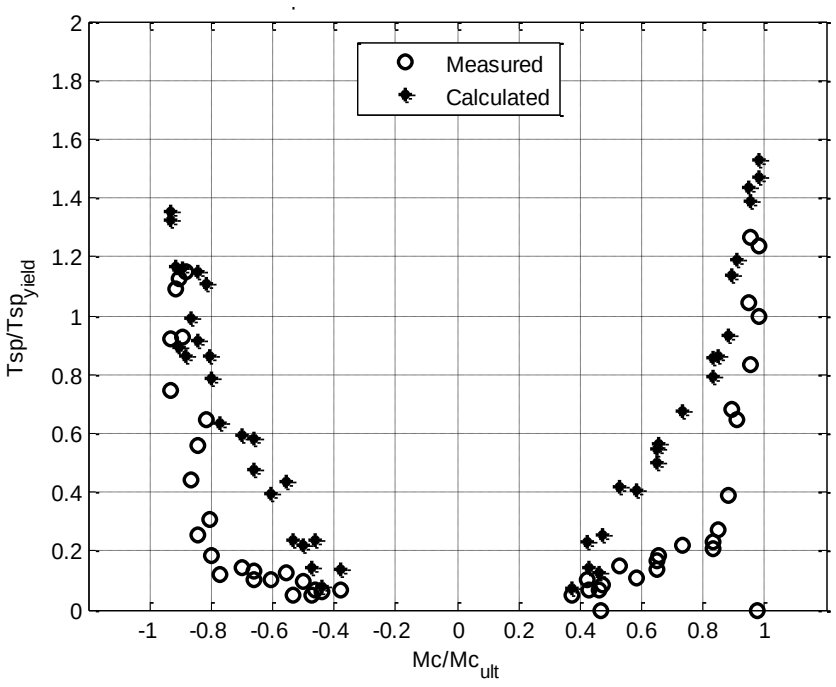

Figure 3.12. Spiral Resultant Force vs. Column Moment – DS-1

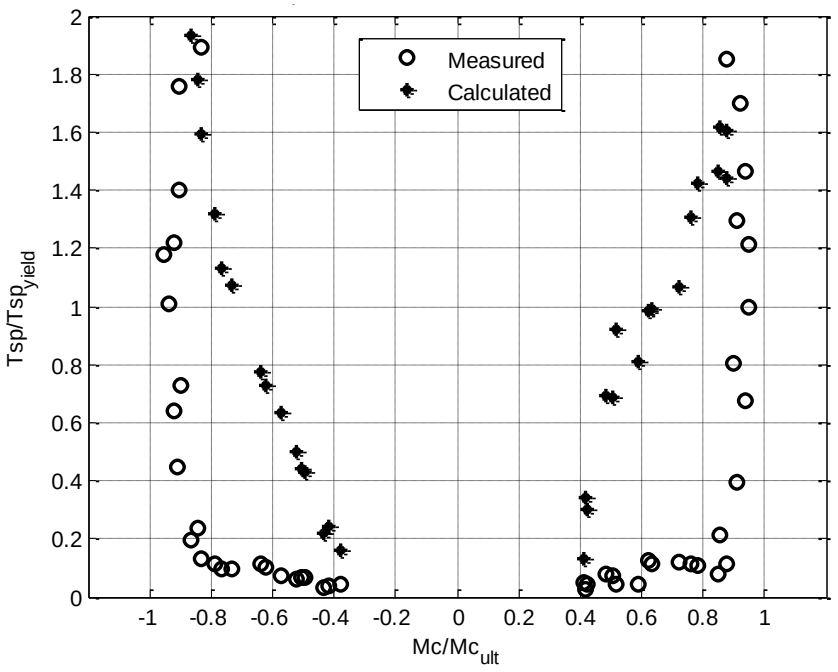

Figure 3-13. Spiral Resultant Force vs. Column Moment – DS-2

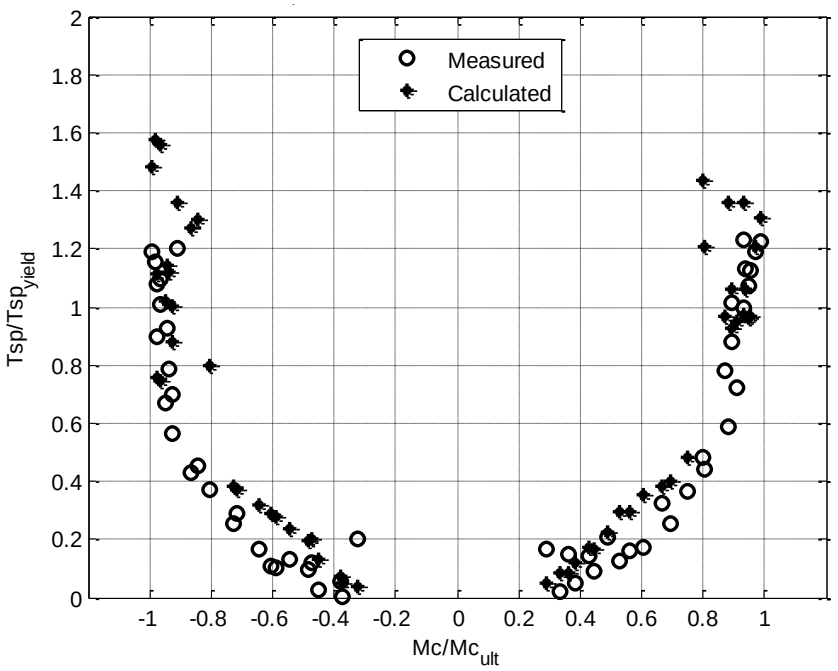

Figure 3-14. Spiral Resultant Force vs. Column Moment – DS-3

CHAPTER 4

EXPERIMENTS AND ANALYSES OF CONCRETE FILLED STEEL TUBE CONNECTIONS

4.1 INTRODUCTION

Concrete filled steel tubes (CFSTs) are composite structural elements which provide large strength and stiffness while permitting accelerated bridge construction (ABC). The steel tube serves as formwork and reinforcement to the concrete fill, negating the need for reinforcing cages, shoring, and temporary formwork. In relation to ABC, the placement of the concrete fill may be further enhanced using self-consolidating concrete (SCC), so that concrete vibration is not required.

The steel tube is placed at the optimal location to resist bending forces, thereby maximizing strength and stiffness while minimizing weight and material requirements. In addition, the steel tube provides optimal confinement and much greater shear strength than spiral reinforcement, which is typically used for circular reinforced concrete columns. In addition, the concrete fill restrains local tube buckling, supports compressive stress demands, and offers large stiffness to meet functionality seismic performance objectives and non-seismic load requirements. Shear stress transfer must occur between the steel tube and concrete fill to ensure full composite action, which increases efficiency, resistance, and ductility, all of which are desirable properties for seismic design (Roeder et al. 1999; Roeder et al. 2009; Roeder et al. 2010; Lehman and Roeder, 2012; Brown et al. 2013).

Although CFSTs offer many advantages in rapid construction and improved structural performance, connections between CFSTs are often different and more complex than those used

in steel or reinforced concrete construction due to the composite nature of CFSTs. Prior numerical and experimental research resulted in straight forward design and corresponding expressions for an embedded column-to-foundation connection (Lehman and Roeder, 2012). Results from that research are presented briefly here. The primary focus of this paper is the development and experimental investigation of robust CFST column-to-cap beam connections capable of sustaining cyclic lateral loads while minimizing damage and degradation. The study focus is on precast bent caps, since this benefits ABC, and practical design expressions are developed for these connections based upon the experimental research.

4.2 CFST COLUMN-TO-FOUNDATION CONNECTION

A foundation connection in which the steel tube is embedded into the foundation concrete has previously been developed, and is illustrated in Fig. 4.1 (Kingsly, 2005; Chronister, 2007; Williams, 2006; Lee, 2011; Lehman and Roeder, 2012). This connection is capable of transferring the plastic moment capacity of the CFST, and can provide large lateral deformation capacities when appropriately designed as is illustrated by hysteresis in Fig. 4.2. The connection employs an annular ring which is welded to the base of the steel tube, and projects both inside and outside of the steel tube to provide anchorage and efficient shear and moment transfer to the surrounding concrete and reinforcement, as is illustrated by the compression struts in Fig. 4.1a. There are no internal shear connectors, dowels, or reinforcing bars penetrating from the tube into the foundation; the force transfer is solely accomplished by the anchorage provided by the tube. The foundation is designed to normal depth, design loads, and flexural reinforcement.

Two methods for constructing the foundation connection have been developed and experimentally evaluated; a monolithic method in which the steel tube and annular ring are temporarily supported in the foundation concrete and the foundation and CFST column are cast

simultaneously and a grouted method in which the construction of foundation and CFST column are isolated (illustrated in Fig. 4.1b). The second method achieves the objectives of ABC by separating the construction of the foundation from the construction of the CFST column. Using this method, the footing is cast with a recess formed by a light weight corrugated pipe with an inner diameter slightly larger than the outer diameter of the annular ring as shown in Fig. 4.1b. The tube and ring are placed into the void after the foundation is cast, and the recess between the tube and corrugated pipe is filled with high strength fiber reinforced grout to anchor the column into the foundation. The fiber reinforced grout used in the connection should be non-shrinkage according to ASTM C 1107, and should meet durability requirements according to ASTM C666 and ASTM C1012. These requirements are specified in NCHRP Report 681 for emulative grouted connections in precast construction (Restrepo et al. 2011).

Detailed information regarding the grout and fiber properties as well as mixing and construction procedures are provided in reference material (Kingsly, 2005; Chronister, 2007; Williams, 2006; Lee, 2011). For both options, the steel tube is filled with low shrinkage self-consolidating concrete to complete the CFST column, and no vibration is required (Lehman and Roeder, 2012).

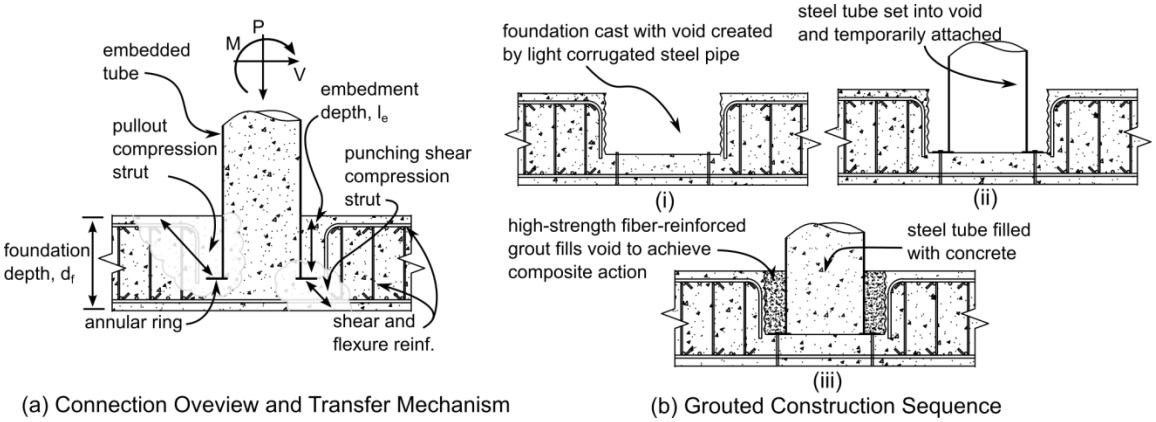

Figure 4.1. CFST Column-to-Foundation Connection

4.2.1 Experimental Behavior

The compilation of the experimental programs to evaluate the CFST column-to-foundation connection consisted of a series of 19 large-scale specimens which simulated approximately a half scale bridge column (Kingsly, 2005; Chronister, 2007; Williams, 2006; Lee, 2011; Lehman and Roeder, 2012). The diameter and thickness of the steel tube in a majority of the specimens were 20-in. and 0.25-in. respectively; resulting in a diameter-to-thickness ratio (*D/t*) of 80. This exceeds the limiting *D/t* ratio specified in ACI 319 (2011), but meets the requirements in the AASHTO LRFD (2015) design specifications and the AISC Steel Construction Manual (2011). The annular ring in all specimens extended 16*t* (4-in.) and 8*t* (2-in.) from the outer and inner diameter of the steel tube respectively. The dimensions of the footing as well as the primary flexure reinforcing were selected to provide adequate strength for the foundation to minimize the influence of footing size on the failure mode, resist M_P of the CFST without yielding, and to represent a scale model of a typical bridge footing. The imposed displacement history for a majority of the specimens was based on the ATC-24 (1992) protocol, and a majority of the specimens were subjected to approximately 10% of the gross compressive load capacity of the CFST column.

As the testing program was so large, only the hysteretic performances of selected specimens are discussed here to demonstrate the influence of tube embedment depth on connection behavior. The moment drift behaviors of inadequately and adequately embedded specimens are shown in Fig. 4.2a and Fig. 4.2b respectively, while typical behaviors and failure modes are shown in Fig. 4.3 (Lehman and Roeder, 2012). The moments have been normalized to the theoretical plastic moment capacity of the CFST component as calculated using the plastic stress distribution method (PSDM), which is shown as a dashed line in each of the subfigures of

Fig. 4.2. This method is illustrated in reference material (AASHTO, 2015). In summary, the ductility of inadequately embedded connections was ultimately limited by foundation damage due to a conical pullout of the CFST from the foundation, as shown in Fig. 4.3a. In general, the failure mode of adequately embedded connections was characterized by ductile tearing of the steel tube which initiated as a result of local tube buckling as is illustrated in Fig. 4.3c. Furthermore, adequately embedded specimens exhibited a minimal decrease in resistance as a result of severe local buckling which generally initiated at around 4% drift, and had virtually no foundation damage at the end of testing as is shown in Fig. 4.3b. The drift levels achieved by the adequately embedded specimens at failure are significantly larger than those observed from similar size reinforced concrete pier and column base connections (Kingsly, 2005; Chronister, 2007; Williams, 2006; Lee, 2011; Lehman and Roeder, 2012).

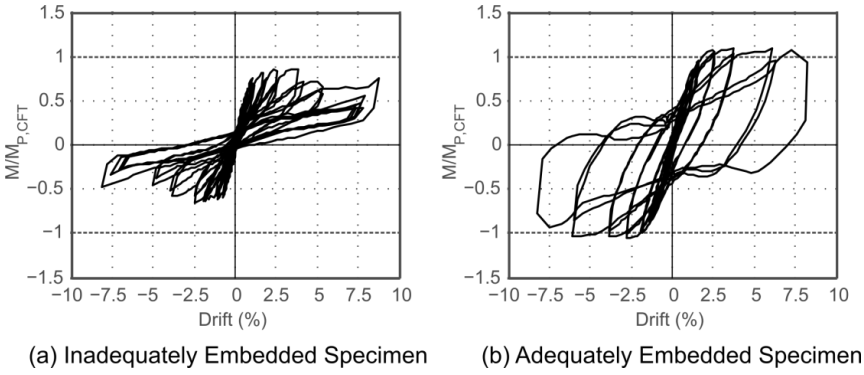

Figure 4.2. Typical Moment-Drift Response from Adequately and Inadequately Embedded Specimens[6]

Figure 4.3. Photos of Foundation Connection Behavior[6]

4.2.2 Design Expressions

The experimental results were used to develop design expressions for a CFST column-to-foundation connection capable of transferring the full moment capacity of the CFST. Specifically, expressions were developed to dimension and detail the annular ring, determine the required embedment depth of the tube to eliminate the conical pullout failure mode, and to determine the required depth of concrete below to the tube to prevent concrete punching failure. These expressions are not discussed here for brevity; however detailed explanations are available in reference material (Lehman and Roeder, 2012).

4.3 CFST COLUMN-TO-CAP BEAM CONNECTION

While the numerical and experimental analyses conducted on the CFST foundation connection resulted in design expressions to support the use of CFST columns in highway bridges, full realization of the system requires the development of a range of cap beam connections. This connection offers unique challenges including congested joint reinforcing and limits on the width and height of the cap beam, which are parameters that have not been previously evaluated. Furthermore, the optimization of ABC requires exploring connections which are compatible with precast superstructure elements. To achieve these objectives, the continuing phase of this research is focused on the development robust CFST cap beam

connections capable of sustaining cyclic lateral load demands while mitigating damage and degradation.

The proposed CFST column-to-cap beam connections are illustrated in Fig. 4.4. There are three connection types: (1) embedded ring connections (Fig. 4.1a), (2) welded dowel connections (Fig. 4.1b), and (3) reinforced concrete connections (Fig. 4.3c). This provides a suite of connections for designers, each option offering advantages as the project may require.

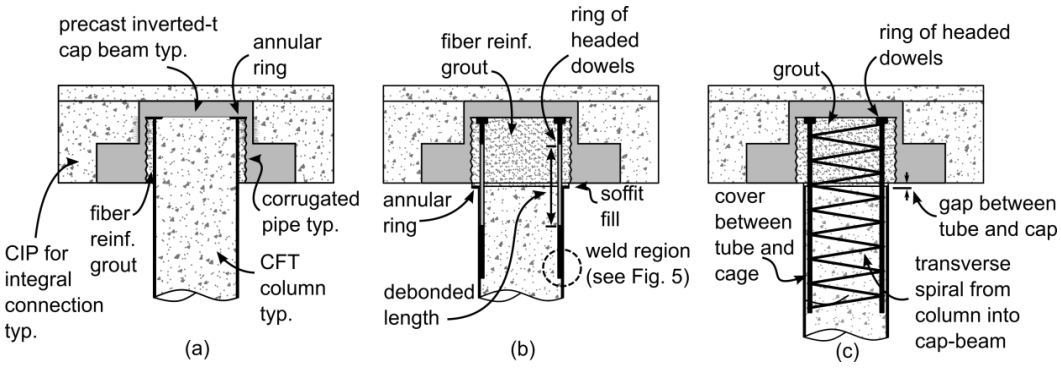

Figure 4.4. Proposed CFST Column-to-Precast Cap Beam Connections. (a) Embedded Ring Connection (ER), (b) Welded Dowel Connection (WD), and (c) Reinforced Concrete Connection (RC)

Fig. 4.4a shows a full strength embedded ring connection (herein referred to as ER); this connection is similar to the embedded flange column-to-foundation connection evaluated in previous research (Lehman and Roeder, 2012). The connection uses a grouted connection detail, with a void cast into a precast cap beam. A circular ring is welded to the steel tube to provide anchorage and transfer stress to the concrete and reinforcing in the cap beam. The flange extends a distance 8 times the thickness of the tube (8t) both inside and outside of the tube. The external projection of 8t is smaller than previous recommendations for the embedded foundation connection (Lehman and Roeder, 2012). The precast cap beam is placed onto the column after

the column is set, and the recess between the tube and corrugated pipe is filled with high strength fiber reinforced grout.

The connections illustrated in Fig. 4.4b – Fig. 4.4d utilize T-headed reinforcing dowels that extend from the CFST column into the cap beam to provide axial, moment, and shear transfer. These connections can be integrated into precast elements using a void similar to that described for the grouted CFST connection as shown in Fig. 4.4b – Fig. 4.4d.

Fig. 4.4b shows a welded dowel connection (herein referred to as WD). The WD connection utilizes headed dowels to resist the flexural demand. The shear transfer to the tube is accomplished by welding the dowels to the steel tube using a flare bevel groove weld as illustrated in Fig. 4.5. The dowels are developed into the cap beam using a high-strength, fiber-reinforced grouted connection. Welding the dowel directly to the tube, as opposed to embedding the dowel directly into the connection maximizes the moment capacity of the dowel connection. A soffit fill depth is included between the steel tube and cap beam. An annular ring with an outer diameter of D+8t is welded to the exterior of the steel tube to increase compressive bearing area on the soffit fill. As illustrated in Fig. 4.4b, the dowels can be de-bonded in the column-to-cap beam interface region to increase the deformation capacity of the connection.

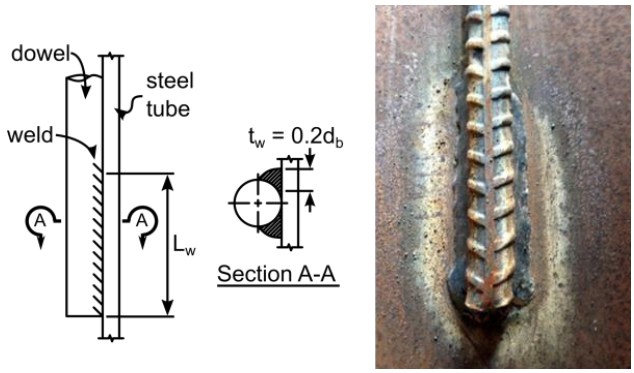

Figure 4.5. Flare Bevel Groove Weld Between Longitudinal Dowel and Steel Tube

Fig. 4.4c shows a reinforced concrete connection (referred to as RC connection) in which a short independent cage for both transverse and longitudinal reinforcing extends from the CFST column into the cap beam, and cover is provided between the reinforcing cage and steel tube within the column. A gap is left between the steel tube and cap beam to help focus the plastic hinging location between the CFST component and the cap beam (Stephens et al. 2015).

4.3.1 Specimen Design

Eight large scale specimens were designed to experimentally evaluate the performance of the proposed connections under constant axial and reversed cyclic lateral loading. Two sets of specimens were designed and constructed; one set to evaluate the performance for loading in the transverse direction of the bridge, and one set to evaluate performance for loading in the longitudinal direction of the bridge. Specimen geometries are illustrated in Fig. 4.6 and Fig. 4.7 for loading in the transverse and longitudinal directions respectively, while specimen cross sections in the connection region are illustrated in Fig. 4.8.

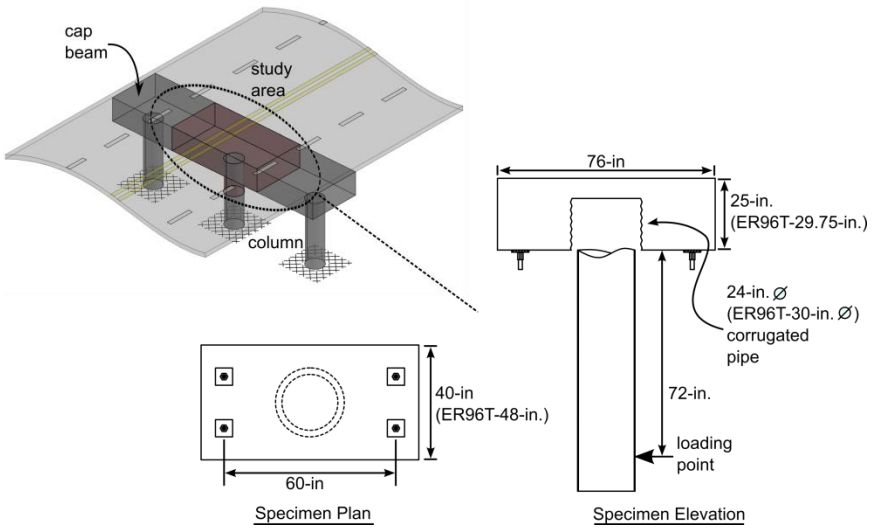

Figure 4.6. Transverse Study Region and Scaled Specimen Geometry.

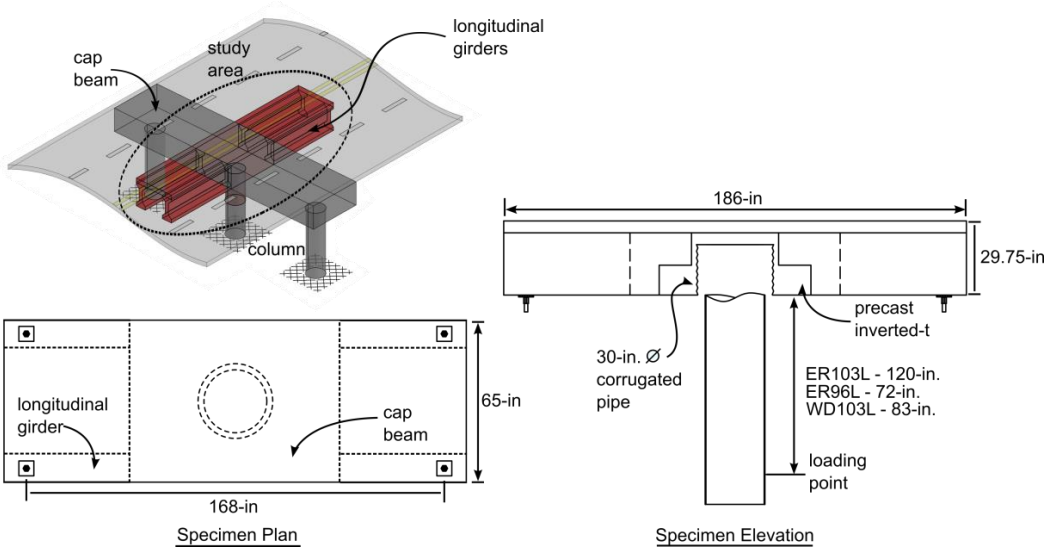

Figure 4.7. Longitudinal Study Region and Scaled Specimen Geometry

Four 20-in. diameter and one 24-in. diameter CFSTs were selected to evaluate the performance of the proposed connections for loading in the transverse direction (resulting in scale factors of 48% and 57%, respectively), while two 25.75-in. CFST and one 24-in. diameter CFST were selected to evaluate performance for loading in the longitudinal direction (resulting in scale factors of 61% and 57%, respectively). All tubes had a thickness of 0.25-in, resulting in D/t ratios of 80, 96, and 103 for the 20-in, 24-in, and 25.75-in. tubes, respectively. Specimen nomenclature used here refers to the connection type, as illustrated in Fig. 4, followed by the D/t ratio, and a letter to denote the direction of loading (T for transverse and L for longitudinal), i.e., ER96T describes an embedded connection with D/t = 96 for loading in the transverse direction of the bridge.

All of the specimens were constructed using pre-cast cap beams cast with a recess formed by light-gauge corrugated metal pipe, and the columns were grouted into place using high strength fiber reinforced grout. The specimens were cantilever columns anchored into a cap beam as illustrated in Fig. 4.6 and Fig. 4.7. Specimen cross sections in the connection region are

illustrated in Fig. 4.8. Joint shear reinforcing in the welded dowel and reinforced concrete connection specimens was scaled from a prototype bridge and checked against the California Department of Transportation Seismic Design Criteria (2013), while vertical shear reinforcing in the joint region of the cap beam for the ER connection was designed according to recommendations provided in reference material[4]. Flexural reinforcement in the cap beam was designed to resist 1.2 times the theoretical flexural strength of the CFST columns.

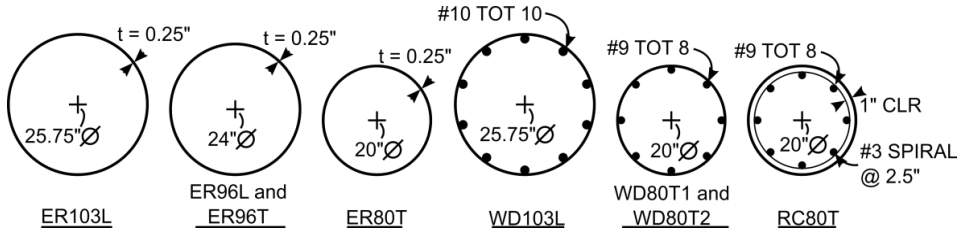

Figure 4.8. Column Cross Sections in Connection Region

4.3.1.1 Embedded Ring (ER) Connection

Two transverse and two longitudinal specimens were designed to evaluate the performance of the proposed ER CFST column-to-cap beam connection. The specimens were designed: (1) to investigate the performance for smaller cap beam widths than had previously been evaluated for the embedded foundation connection, (2) to evaluate a smaller exterior annular ring projection of 8t (in contrast to 16t that had been used on the prior foundation connections studied), (3) to evaluate the influence of using API or ASTM grade tube steel, (4) to compare a straight seam and spirally welded tube, and (5) to evaluate the performance for loading in the transverse and longitudinal direction of the bridge.

Specimen ER80T was designed with embedment depth of 18-in. (0.9D), and utilized a 61-ksi ASTM A1018 spiral welded steel tube with an annular ring with a 2-in. projection both inside and outside of the tube. Specimens ER96T and ER96L were embedded 20-in (0.83D) into the cap beam (note the lesser relative embedment depth was possible because of the lower steel

strength), and both utilized a 53-ksi API 5L X-42 grade straight seam tube with an annular ring that projected 51-mm (2-in.) inside and outside of the tube. Specimen ER103L was embedded 20.25-in. (0.8D) into the cap beam, and utilized a 69.3-ksi ASTM A1018 spiral welded steel tube with an annular ring with a projection of 2-in. inside and outside of the tube.

4.3.1.2 Welded Dowel (WD) Connection

Three specimens were designed using the welded dowel connection detail: one specimen with fully bonded bars (WD80T1), and two specimens with bars de-bonded along the length (WD80T2 and WD103L). In all cases, the longitudinal reinforcing in the connection region was selected with a target longitudinal reinforcing ratio of 3%, resulting in eight evenly distributed No. 9 bars in WD80T1 and WD80T2 and ten evenly distributed No. 11 bars in WD103L as illustrated in Fig. 4.8. The bars in all welded dowel specimens were embedded $12d_b$ into the cap beam per ACI 318 requirements for the development of headed reinforcing bars (ACI, 2011), and $24d_b$ into the CFST column. The bars were welded to the inside of the steel tubes using flare bevel groove welds formed by requirements of AWS D1.4 designed to exceed F_{ub}, where F_{ub} is the ultimate steel strength of the reinforcing bars. All of the specimens used flanges that projected 2-in. from the exterior of the steel tube and a 1-in. thick soffit fill, which extended below the surface of the cap beam. Specimen WD103L also included transverse No. 5 hoops with the intention of providing additional confinement to the soffit fill and joint region. PVC pipe was used to de-bond the longitudinal reinforcing bars in specimens WD80T2 and WD103L for lengths of 22-in. and 24-in., respectively. The de-bonded lengths were calculated using a moment-curvature analysis to achieve a connection rotation demand of 10% drift prior to fracture of the longitudinal reinforcing.

4.3.1.3 Reinforced Concrete (RC) Connection

One specimen (RC80T) was designed to evaluate the behavior of the reinforced concrete connection. As illustrated in Fig. 4.8, the longitudinal reinforcement consisted of eight evenly distributed No. 9 headed bars in an effort to achieve a longitudinal reinforcing ratio of 3%, and to allow for comparison to the welded dowel connections. The bars were embedded $12d_b$ into the cap beam per the ACI 318 (2011) development requirements for headed reinforcing, and $30d_b$ into the CFST column per development requirements for deformed bars. Transverse column reinforcing was scaled from the prototype column, resulting in a No. 3 spiral at a spacing of 2.5-in. as shown in Fig. 4.8. A clear cover of 1-in. was provided between the steel tube and the transverse reinforcing.

4.3.2 Numerical Analysis

The commercially available finite element analysis software ABAQUS was used to perform a preliminary series of nonlinear analyses on the ER, WD, and the RC cap beam connections with 20-in. diameter tubes with 0.25-in. wall thickness. An overview of the numerical model is shown in Fig. 4.9. Model geometry included the CFT column-to-cap beam connection, the CFT column, and the reinforced concrete cap beam. A half model was developed taking advantage of symmetry in the plane parallel to the direction of loading and the center of the specimen; this increased computational efficiency. The CFT column was modeled using 3-dimensional elements for a length beyond the plastic hinge length of the column. The remainder of the length was modeled using the ABAQUS MPC constraint tied to a reference point. The nodes at the top of the cap beam were restrained to simulate the boundary conditions of experimental tests, and lateral loading was applied by assigning monotonic displacements Δ_X along the x-axis to the reference point. A distributed axial load consisting of 10% the crushing

load of the CFT was applied to the bottom of the concrete and steel tube using the pressure load option in ABAQUS.

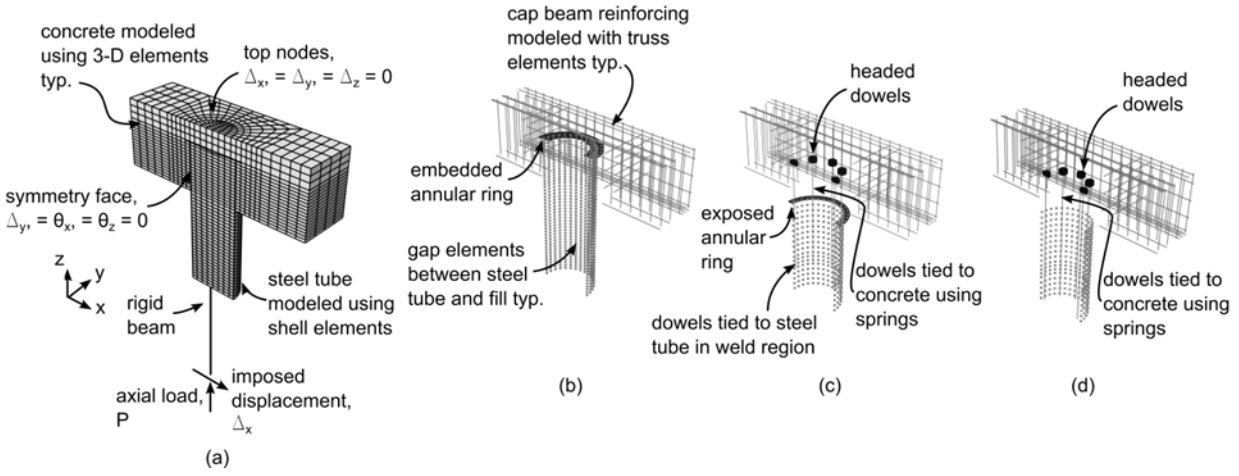

Figure 4.9. (a) Numerical Model Overview, (b) ER Connection, (c) WD Connection, and (d) RC Connection.

Four-node shell elements with reduced integration (ABAQUS element type S4R), 2-node truss elements (ABAQUS element type T3D2), 2-node beam elements (ABAQUS element type B31), and 8-node solid elements with reduced integration (ABAQUS element type C3D8R) were used to model steel tube, cap beam reinforcing steel, connection reinforcing steel (for WRC, WRCUB, and EMBRC), and concrete elements, respectively. Gap elements were used at every nodal point that was geometrically common the steel tube and concrete fill elements to simulate bond stress between the concrete by combining the confining contact stress with a coefficient of friction to develop shear stresses at the interface; penetration of the concrete element by the steel element was prevented. The reinforcing steel and concrete components in the cap beam were spatially assembled, and interactive constraint relationships were defined using the ABAQUS Embedded constraint to perfectly embed the cap beam reinforcement in the cap beam concrete.

4.3.2.1 Connection Type

Moment-drift relationships for the differing connection types are plotted in Fig. 4.10a, while inelastic deformations at 10% drift are plotted in Fig. 4.10b. The moments have been normalized to the plastic moment capacity of the CFT calculated using the PSDM to allow for comparison. The plastic strain for all connection types was isolated to the connection region with limited inelastic deformation in the cap beam. Although the yielding mechanism in the WD and RC connections was characterized by inelastic deformation in the column reinforcing, these connections did not achieve the plastic moment capacity of the CFT due to lower effective longitudinal reinforcing ratios. Additionally, the RC connection did not provide as much strength as the WD connections due to a smaller moment arm.

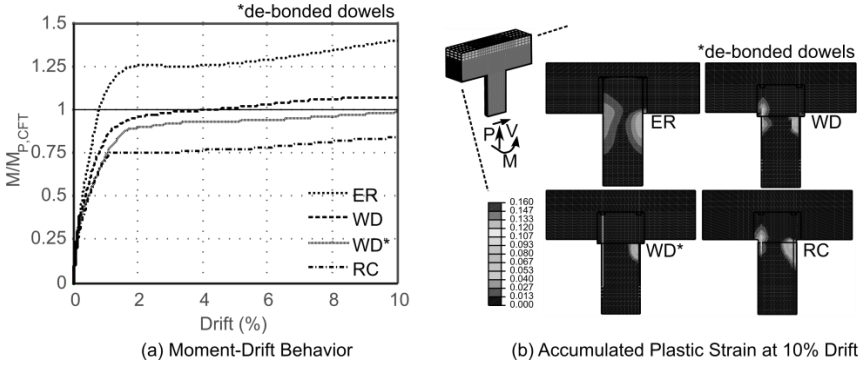

Figure 4.10. (a) Numerical Moment-Drift Behaviors and (b) Accumulated Plastic Concrete Strain at 10% Drift for the Proposed Connection Types

4.3.3 Experiments

The proposed connection types were experimentally evaluated in the structural testing lab at the University of Washington (Stephens et al. 2015). Specimen geometry was consistent with that defined in Fig. 4.6 and Fig. 4.7. The specimens were tested using a self-reacting test frame with a horizontal actuator to apply the lateral load and a Baldwin Universal Testing Machine (UTM) to apply a constant vertical lateral load as shown in Fig. 4.11.

The imposed displacement protocol was based on the ATC-24 (1992) protocol, and the specimens were subjected to 10% of the gross compressive load capacity of the CFST column. The specimens were instrumented using strain gages, linear potentiometers, string potentiometers, and an Optotrak motion capture system, however only the global moment-drift behavior measured using a load cell on the horizontal actuator and a string potentiometer placed at the center of loading is presented here. The location of this string potentiometer is indicated in Fig. 4.11. All specimens were tested in an inverted configuration due to constraints of the available testing apparatus.

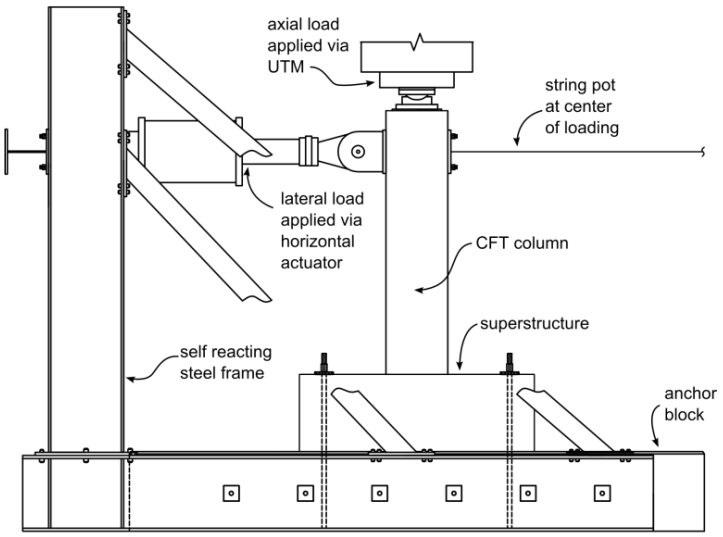

Figure 4.11. Test Apparatus

The moment drift behaviors of select specimens are plotted in Fig. 4.12, while the failure modes of select specimens are illustrated in Fig. 4.13. Only a brief description of the experimental behavior is presented here for brevity; more detailed descriptions are provided in reference material (Stephens et al. 2015). The moments have been normalized to the theoretical plastic moment capacity of the CFST calculated using the PSDM to allow for comparison of the specimens.

The ER connections exhibited larger stiffness and comparable strength to the WD connections. The larger stiffness of the embedded connection specimens is a result of the location of the tube as well as the confinement of the concrete fill. The comparable strengths are a result of the fact that the ER and WD connections had similar effective reinforcing ratios and moment arms. The RC connection developed significantly less resistance than the RC or WD connections due to a significantly smaller moment arm. The failure mode of all the ER connections was characterized by ductile tearing of the steel tube near the CFST column-to-cap beam interface as illustrated in Fig. 4.13a. These connections exhibited local buckling near this interface at drift ratios ranging from 3%-4%, however this did not influence the lateral load carrying capacity of the CFST column. In general, the welded dowel connections exhibited large ductility, however the failure modes of WD80T1 and WD80T2 was ultimately characterized by cap beam failure as illustrated in Fig. 4.13b. WD103L was cycled to 12% drift with no decrease in resistance or damage to the superstructure. The final state of specimen WD103L is illustrated in Fig. 4.13c. No bar buckling and only limited soffit crushing was observed in this specimen, as the transverse hoops in the joint region provided confinement. Note that transverse hoops were not included in the WD80T1 and WD80T2 specimens. The failure mode of the EDC connection was characterized by bar fracture and soffit crushing as illustrated in Fig. 4.13d, as six out of the eight connection bars fractured during cycling from 10% to 12% drift, and limited cap beam damage was observed.

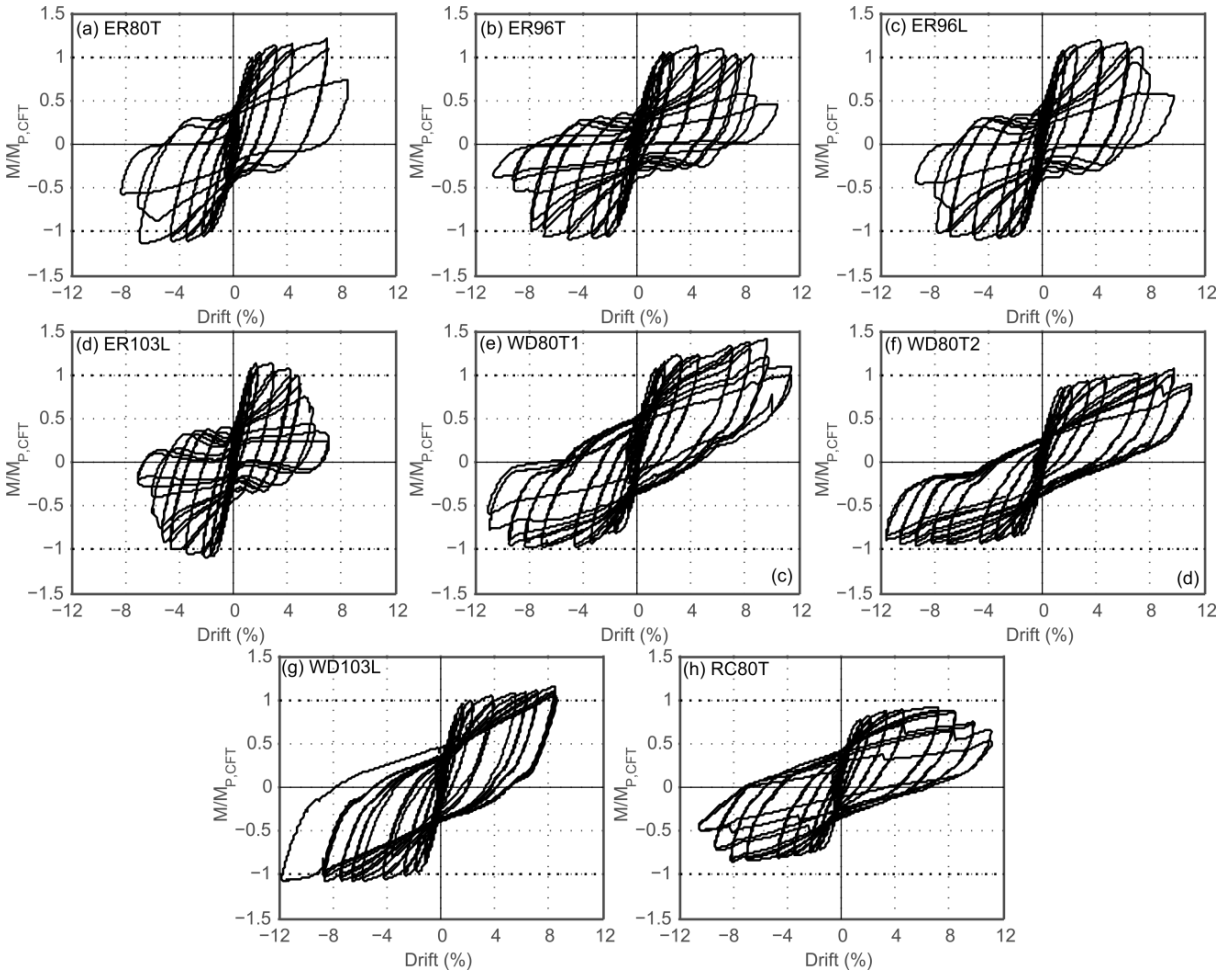

Figure 4.12. Experimental Moment-Drift Behaviors

Figure 4.13. Final State of Select Specimens

CHAPTER 5

DESIGN EXPRESSIONS FOR CFST CONNECTIONS

The experimental results and observations from the CFST tests were used to develop practical engineering expressions for the proposed CFST column-to-cap beam connections. The connection should be designed as one of the following options:

1. An embedded CFST connection (ER connection) in which the CFST column is embedded into the cap beam as illustrated in Fig. 4.4a and Fig. 5.1.
2. A welded dowel connection (WD connection) in which a ring of partially deboned vertical headed reinforcing bars are welded inside the CFST column and extend into the cap beam as illustrated in Fig. 4.4b and Fig. 5.4.
3. A grouted dowel connection (RC connection) in which a ring of headed reinforcing bars is developed into the steel tube and extend into the cap beam.

Each of these options can be employed using cast-in-place (CIP) or precast super-structure cap beam. For precast construction, a void must be included in the precast elements through use of a corrugated pipe, which meets the specifications outlined below. The following sections summarize design expressions for the ER and WD connection types. Design of the RC connection is very similar to that of a jacked reinforced concrete column, and has thus been omitted here. Additional information on design can be found in reference material (Stephens et al. 2015).

5.1 MATERIALS

Materials for the specified connections shall conform to the Caltrans standards (2013), with several specific provisions included in this section.

5.1.1 Grout

When precast components are used, the fiber-reinforced grout consisting of prepackaged, cementitious grout and meeting ASTM C-1107 for grades A, B, and C non-shrink grout is used. The grout conforms to several additional performance requirements including compressive strength, compatibility, constructability, and durability. The 28-day grout strength f'_g must exceed f'_c of the surrounding concrete components. Grout using metallic formulations shall not be permitted, and grout shall be free of chlorides. No additives should be added to pre-packaged grout. These requirements ensure the grout has properties that provide adequate strength and longevity. These requirements adapted from recommendations provided in NCHRP Report 651 (Restrepo et al. 2011).

5.1.2 Fiber Reinforcing

Macro polypropylene fiber with a minimum volume of 0.2% is included to provide crack resistance and bounding characteristics between the tube and corrugated metal duct. Test results to date have not evaluated the use of alternative fibers such as steel fibers.

5.1.3 Corrugated Metal Duct

Corrugated metal ducts are used to provide voids in precast components. The ducts are galvanized steel according to ASTM A653. Duct diameter is selected based on construction tolerances. Plastic ducts should not be used as the purpose of the ducts it to be a bond crack arrestor, act as confinement and provide shear transfer from the grout to the outer concrete. The use of corrugated metal ducts for grouted connections is supported by this research as well as a wealth of seismic precast connection data (Lehman and Roeder, 2012; Restrepo et al. 2011).

5.1.4 Reinforcement

Reinforcing in the connection region shall conform to ASTM A706 Gr. 60 (or Gr. 80 if allowed) requirements for weldable reinforcing. ASTM A706 places restrictions on the chemical composition of reinforcing bars to enhance welding properties.

5.1.5 CFST Tube Steel

Steel tubes may either be straight seam or spiral welded and must conform to either ASTM 1018 or API 5L requirements. Spiral welded tubes must be welded using a double submerged arc welding process, and weld metal properties must match properties of the base metal and meet minimum toughness requirements of AISC demand critical welds[13].

Selection of tube material designation (ASTM 1018 or API 5L) plays a role in the ductility of the full strength embedded CFT connection. API 5L grade steel has more strict requirements regarding chemical composition than ASTM 1018 steel, and can therefore provide additional ductility for both spiral welded and straight seam tubes (Stephens et al. 2015).

5.2 EMBEDDED RING CONNECTION

The embedded ring connection utilizes a CFST fully embedded into the cap beam. The CFST pier or column controls the strength and ductility of this connection type, not the cap beam or other superstructure components. The precast cap is placed on the column after the concrete fill is set, and the recess between the tube and corrugated pipe is filled with high strength fiber reinforced grout as shown in Fig. 5.1.

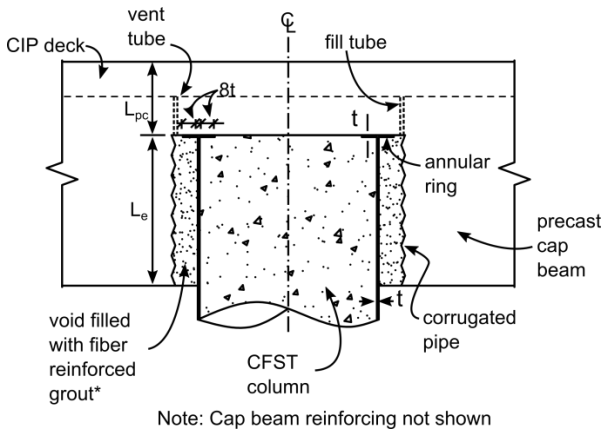

Figure 5.1. Embedded Ring Connection

5.2.1 Annular Ring

The annular ring is welded to tube using complete joint penetration welds or fillet welds on both the inside and outside of the column designed to transfer the full strength of the tube to provide anchorage and stress transfer. The ring is made of steel of the same thickness and similar yield stress as the steel tube. The ring extends into and out from the tube 8 times the tube thickness to provide adequate anchorage as shown in Fig. 5.1.

5.2.2 Embedment Depth

The required embedment depth, L_e, of the CFST was determined using a conical pullout model discussed in detail in reference material (Stephens et al. 2015). The required embedment depth to eliminate the potential for cap beam failure is given in Equation 5.1 as:

$$L_e \geq \sqrt{\frac{D_o^2}{4} + \frac{DtF_{u,st}}{6\sqrt{f'_{c,cap}}}} - \frac{D_o}{2} \ (psi) \qquad [5.1]$$

where D_o is the outside diameter of the corrugated pipe, and D, t, and $F_{u,st}$ are the diameter, thickness, and ultimate stress of the steel tube, and $f'_{c,cap}$ is the compressive strength of the cap beam concrete in psi. The embedded depth, L_e, is illustrated in Fig. 5.1.

5.2.3 Punching Shear

Adequate concrete depth, L_{pc}, must be provided above the tube to eliminate the potential for punching shear failure in the cap beam as shown in Fig. 5.1. The ACI 318 (2011) provisions for footings in single shear were used as a basis to develop an expression for the minimum depth above the embedded CFST to avoid this failure mode. This expression is given in Equation 5.2 as:

$$L_{pc} \geq \sqrt{\frac{D_o^2}{4} + \frac{C_c + C_s}{6\sqrt{f'_{c,cap}}}} - \frac{D}{2} - L_e \ (psi) \qquad [5.2]$$

where C_c and C_s are the compressive forces in the concrete and steel due to the combined axial load and bending moment as computed by the PSDM.

5.2.4 Cap Beam Flexural Reinforcing

Longitudinal flexural reinforcing in the column region is required to resist $1.25M_{p,CFST}$ to ensure the cap beam does not yield. Longitudinal flexural reinforcing is spaced uniformly across the width of the cap beam. To ensure continuity, a minimum of one layer of upper reinforcing must pass above the embedded CFST in the cap beam as illustrated in Fig. 5.2. Some longitudinal reinforcing in the bottom layer will be interrupted by the embedded corrugated pipe. The bottom layer of flexural reinforcing not interrupted by the corrugate pipe shall be designed to resist $1.25M_p$ of the CFST column. Interrupted bars should still be included as shown in Fig. 5.2.

5.2.5 Joint Region Shear Reinforcing

Vertical reinforcing, A_s^{jv}, shall be included in the joint region according to Equation 5.3, where A_{st} is the total area of the steel tube embedded into the cap beam, and A_s^{jv} is the total area of vertical reinforcing required within a distance L_e from the outer diameter of the corrugated pipe when a precast cap beam is used. Derivation of this equation is given in reference material (Stephens et al. 2015).

$$A_s^{jv} = 0.65A_{st} \quad [5.3]$$

Vertical stirrups or ties are distributed uniformly within a distance $D/2+L_E$ extending from the column centerline as shown in Fig. 5.3a. These stirrups can be used to meet other requirements documented elsewhere including shear in the bent cap.

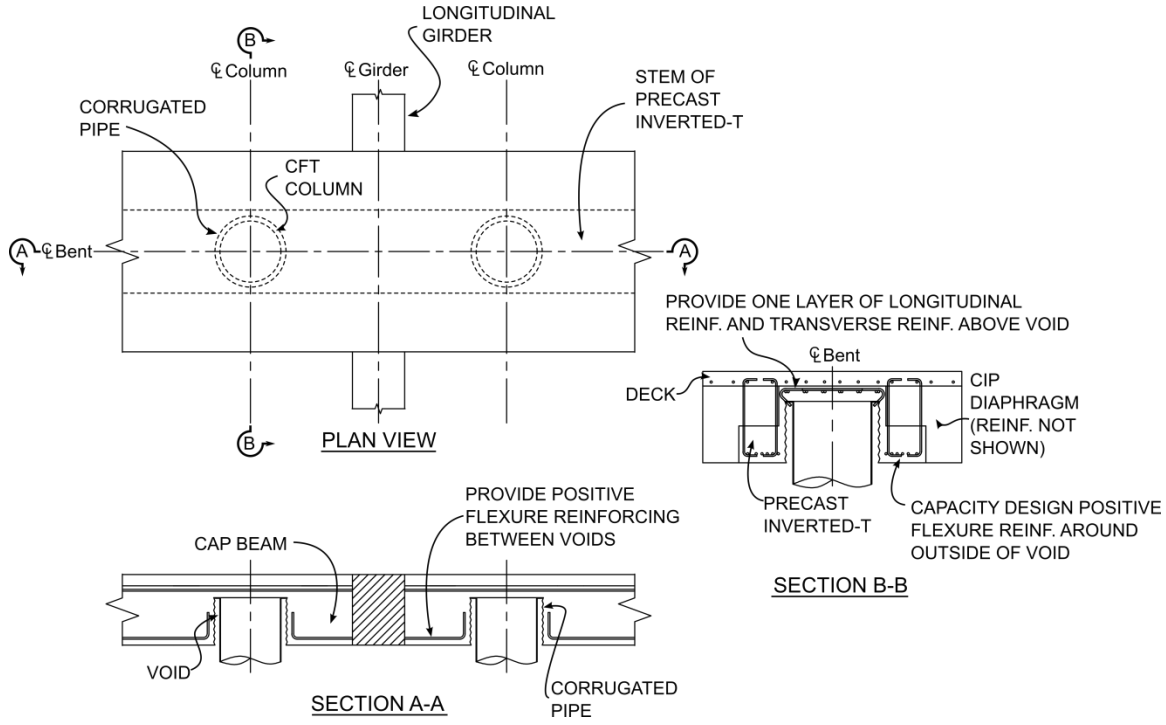

Figure 5.2. Cap Beam Details for Embedded Connection

5.2.6 Joint Region Horizontal Stirrups

Horizontal stirrups or ties shall be placed transversely around the vertical stirrups or ties in two or more intermediate layers spaced vertically at not more than 18-in apart. The horizontal reinforcing area, A_s^{jh}, is determined using Equation 5.4 where A_{st} is the area of the steel tube embedded into the cap beam. The horizontal reinforcing shall be placed within a distance $D/2+L_E$ extending from the column centerline as illustrated in Fig. 5.3b.

$$A_S^{jh} = 0.1 \times A_{st} \quad [5.4]$$

In addition, the top layer of transverse reinforcing should continue across top of the void in the cap beam as shown in section B-B in Fig. 5.2.

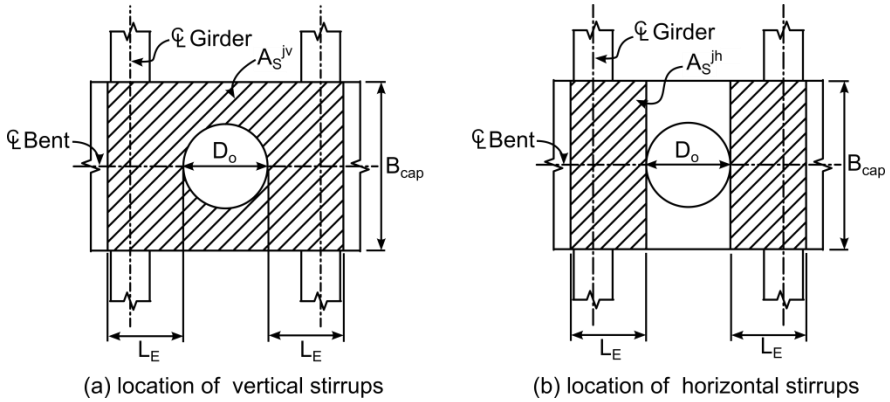

Figure 5.3. Required Location of (a) Vertical and (b) Horizontal Stirrups for the Embedded Ring Connection

5.3 WELDED DOWEL CONNECTION

The welded dowel connection utilizes a ring of headed reinforcing bars that are welded into the tube and developed into the cap beam as illustrated in Fig. 5.4. The strength is controlled by the reinforcing ratio of the longitudinal reinforcing which extends from the column into the

cap beam. The welded detail is designed to carry the full strength of the reinforcing bar. The advantage of this connection is a shorter embedment length into the CFST column and a maximized moment arm. Design of this connection shall conform to requirements in the Caltrans standards (Caltrans, 2013), with several specific provisions included below.

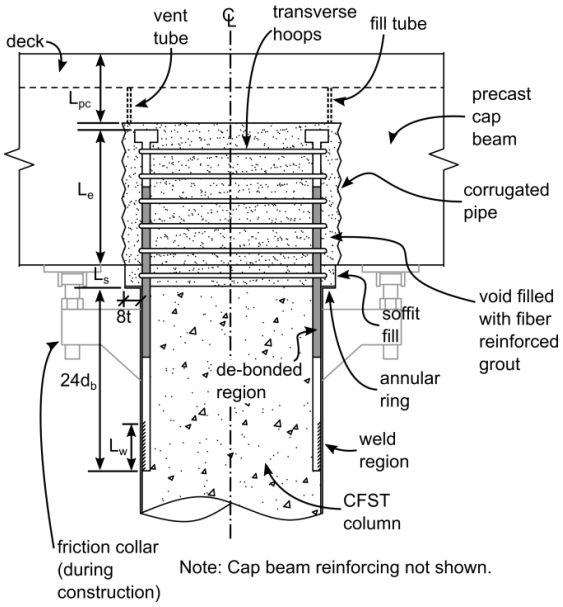

Figure 5.4. Welded Dowel Connection

5.3.1 Annular Ring

The annular ring is welded to end of the steel tube to provide a larger area to transfer compressive stress from the steel tube into the soffit fill. In this connection the ring does not transfer tensile stresses but does provide some compressive force transfer. The ring is made from steel of the same thickness and yield strength as the steel tube. The ring projects outside of the steel tube a distance 8 times the thickness of the steel tube as illustrated in Fig. 5.4.

5.3.2 Length Dowels Extend into the Cap Beam and Column

The headed reinforcing extends into the cap beam to fully develop the longitudinal dowels while also eliminating the potential for a conical pullout failure. The headed dowels must

extend into the cap beam for the largest length calculated using Equation 5.5 and Equation 5.6. Equation 5.5 defines the required development length to develop reinforcing bars with mechanical anchors. Note that ACI is referenced because neither AASHTO (2015) nor the Caltrans SDC (2013) provide development expressions for headed bars. Equation 5.6 defines the required embedment length to eliminate a conical pullout failure similar to the tube embedment depth requirement defined in Equation 5.1. The derivation of Equation 6 is provided in reference material (Stephens et al. 2015).

$$L_e \geq \frac{0.016\psi_e F_{y,b}}{\sqrt{f'_g}} d_b \qquad [5.5]$$

$$L_e \geq \sqrt{\frac{D^2}{4} + \frac{1.2 * F_{y,b} * A_{st,b}}{6\pi\sqrt{f'_{cc}}}} - \frac{D}{2} \qquad [5.6]$$

The longitudinal dowels must extend into the CFST for a distance adequate to develop the full strength of the dowels while limiting damage to the concrete fill. Results from welded dowel pullout tests (discussed in references (Stephens et al. 2015)) suggest that the embedment can be as low as $18d_b$ for full dowel development, however a distance of $24d_b$ is recommended here to provide a reasonable factor of safety.

5.3.3 Vertical and Horizontal Joint Region Reinforcing

Cap beam detailing requirements specified in the California Department of Transportation Seismic Design Criteria V. 1.6 (2013) should be followed when designing the welded dowel connection.

5.3.4 Soffit Fill Depth

The soffit fill depth, L_s, is calculated according to Equation 5.7 to ensure that the annular ring does not come in to contact with the bottom of the cap beam at the maximum expected drift angle, θ_u where D is the outer diameter of the annular ring. This depth is illustrated in Fig. 5.4.

$$L_s \geq \sin(\theta_u)\left(\frac{D}{2} + 8t\right) \quad [5.7]$$

5.3.5 Dowel De-bonded Length

Longitudinal dowels should be de-bonded from the concrete in the connection region with the intent of increasing connection ductility. The required de-bonded length to achieve a pre-determined connection rotation, θ_u, prior to bar fracture is calculated using Equation 5.8 or 5.9, where ϕ_u is a curvature limit corresponding to a maximum steel strain as obtained from a moment-curvature analysis. Half of the de-bonded length extends into the cap beam, and half of the de-bonded length extends into the CFST column as illustrated in Fig. 5.5.

$$L_{db} = \frac{\theta_u}{\phi_u} \quad [5.8]$$

$$L_{db} = \frac{\tan\theta(D - t - d_b/2)}{0.7\varepsilon_u} \quad [5.9]$$

Equation 5.9 is a simplified method for estimating the required de-bonded length of the longitudinal reinforcing to achieve a pre-determined drift ratio prior to bar fracture. Although this method does not require a moment curvature analysis, it results in larger de-bonded lengths than those calculated using a moment-curvature analysis, as required in Equation 5.8.

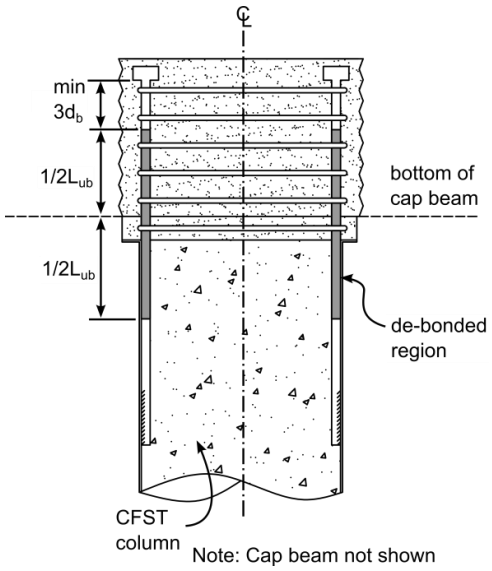

Figure 5.5. Welded Dowel Connection Debonding Dimensions

5.3.6 Dowel-to-Steel Tube Welds

Longitudinal dowels are welded to the inside of the steel tube using flare bevel groove welds on both sides of the dowels, as illustrated in Fig. 4.5. The required weld lengths to develop the rupture capacity of the longitudinal dowels are specified in Equation 5.10 and are based on typical weld limit states for flare bevel groove welds where A_b is the area of the longitudinal dowel, $F_{y,b}$ is the yield strength of the longitudinal dowel, and F_{EXX} is the tensile strength of the weld metal. Equation 5.10a is based on failure of the weld metal, Equation 5.10b is based on yielding of the tube steel, and Equation 5.10c is based on rupture of the tube steel. A strength reduction factor of 0.9 has been included for yielding limit states in Equations 5.10a and 5.10b, while a strength reduction factor of 0.75 has been included based on a tube steel rupture limit state in Equation 5.10c.

$$L_w \geq \frac{5.6 A_b F_{y,b}}{F_{EXX} d_b} \qquad [5.10a]$$

$$L_w \geq \frac{0.83 A_b F_{y,b}}{F_{y,st} t} \quad [5.10b]$$

$$L_w \geq \frac{1.11 A_b F_{y,b}}{F_{u,st} t} \quad [5.10c]$$

5.3.7 Use of Spiral or Hoop Reinforcement in the Joint Region

Transverse reinforcing in the form of spiral or individual hoops should be included around the longitudinal dowels which extend into the cap beam according to requirements in the California Department of Transportation Seismic Design Criteria V. 1.6. At least one hoop should be placed in the soffit fill depth if individual hoops are used as shown in Fig. 5.4. This reinforcing acts to confine the grout in the joint region and limit buckling of the longitudinal dowels[16].

5.4 CONCLUSIONS AND FUTURE WORK

An embedded CFST column-to-foundation connection in which the steel tube is grouted into the foundation concrete was briefly introduced. Experimental research showed that this connection is capable of transferring the plastic moment capacity of the CFST column while limiting damage to the foundation. The experiments provided valuable information and resulted in straight forward and practical design expressions for an embedded foundation connection.

Several new CFST column-to-cap beam connections were proposed and experimentally studied using increasing cyclic deformations. These connections included (1) an embedded ring connection in which an annular ring is welded to the top of the steel tube and embedded into the cap beam (2) a welded dowel connection in which a ring of headed dowels is welded to the inside of the steel tube and developed into the cap beam, and (3) an reinforced concrete connection in which a traditional reinforcing cage consisting of a ring of headed dowels with

transverse reinforcing is developed into the CFST column and cap beam. All of the connections were demonstrated using a grouted connection detail, which can be integrated with precast cap beam components for ABC. A series of large scale specimens were tested to evaluate the behavior of the different connection types. The experimental results suggest that all of the connection types can achieve strength and ductility objectives within the unique constraints of a precast cap beam, and practical engineering expressions were developed for the proposed connections.

Additional research should be conducted to further refine the design expressions, and evaluate the behavior of the connections for a much wider range of parameters. An evaluation of possible repair methods would be beneficial to demonstrate the advantages of using CFSTs in highway bridge construction. Thus four primary areas of future work are recommended:

1) Utilize the detailed finite element models developed for the initial connection evaluation to conduct extensive parameter studies on the proposed connections.
2) Evaluate repair strategies for columns which have been moderately damaged following lateral load events.
3) Develop additional connections such that CFSTs are more versatile for bridge construction; specifically a CFST-to-pile connection is needed.
4) CFSTs should have larger torsional strength and deformability relative to RC columns. A research program aimed at evaluating the response of CFST columns and connections subjected to combined torsional, shear, flexure and axial loading is needed. In addition this program should develop a connection capable of transferring torsion to the superstructure for skewed bridges.

CHAPTER 6

SEISMIC PERFORMANCE OF HIGH-STRENGTH STEEL RC BRIDGE COLUMNS

This chapter presents results of a testing program developed to assess the performance of circular reinforced concrete (RC) bridge columns constructed with ASTM A706 Grade 80 [550] high-strength steel (HSS) reinforcement. Two pairs of columns were subjected (four columns in total). to lateral cyclic loading to determine the effects of steel reinforcement grade and of moment-shear span ratio on column performance. All four columns were designed to have similar nominal bending moment capacities, even though each pair consisted of one column constructed with Grade 80 [550] HSS reinforcement and a control column constructed with Grade 60 [420] reinforcement. The first pair had a moment-shear span ratio of six (6) while the second pair had a moment-shear span ratio of three (3). Results indicate that even though columns constructed with Grade 80 [550] reinforcement exhibited lower hysteretic energy dissipation than the control columns, the columns constructed with HSS reinforcement achieved similar resistance, similar peak lateral displacements, and similar curvature ductility values when compared with the control columns constructed with Grade 60 [420] reinforcement. Results also indicate that, independently of the steel grade, as the moment-shear span ratio decreases, the maximum drift ratio decreases, even though the displacement ductility increased.

6.1 INTRODUCTION

In seismic regions, reinforcement congestion can present a significant challenge during construction of bridge structural members (Gustafson 2010; Risser and Hoffman 2014). Since the use of higher yield strength reinforcing steels could reduce reinforcement congestion, in

2012, the American Association of State Highway and Transportation Officials (AASHTO) and several US State Highway Agencies (SHAs) allowed the use of Grade 80 [550] reinforcement for designing and constructing all bridge structural members except compression members designed to form a plastic hinges, such as bridge columns. Even though the 7th Edition of AASHTO LRFD Bridge Design Specifications (AASHTO 2014, section 5.4.3.3), allows State Highway Agencies (SHA) to approve the use of Grade 80 reinforcement, the lack of experimental testing results makes it difficult for SHAs to have a sound support for their decisions. The main reasons for the restrictions placed on the use of this type of high-strength steel (HSS) reinforcement are due to the lack of experimental data on columns constructed with ASTM A706 Grade 80 [550] HSS reinforcement, and due to the known fact that increasing yield strength typically results in decreased material strain ductility. In addition, designers are reluctant to specify Grade 80 [550] HSS reinforcement in projects because it can currently only be used in certain bridge structural members and potential errors in placement could arise, i.e., placing Grade 60 [420] reinforcement where Grade 80 [550] reinforcement is required or vice-versa.

Even with the potential benefits of HSS reinforcement identified almost 40 years ago (Gustafson 2010), limited research has been performed on the seismic performance on compression members constructed with HSS reinforcement. Review of the literature (e.g. Rautenberg et al. 2010) and of the PEER column database (Berry and Eberhard 2008) indicates that limited tests have been performed using Grade 80 [550] HSS reinforcement. Furthermore, research addressing the effects of moment-shear span ratio on the performance of columns using HSS reinforcement was found through studies with conventional reinforcing steel grades. For example, Priestley and Park (1987) performed a large set of column tests with different cross-section shapes, and their testing results indicated that the ductility of short columns, with an

aspect ratio of 2, was larger than that of the columns with an aspect ratio of 4, leading to the conclusion that displacement ductility capacity decreases as the aspect ratio of the column increases. Lehman et al. (2004) evaluated the seismic performance of ten (10) RC columns with four different aspect ratios. The experimental results reported by Lehman et al. (2004) indicated that as the aspect ratio increased (i) the yield drift ratio increased, (ii) the drift ratio when initial spalling occurred increased, and (iii) the drift ratio level when reinforcing bar buckling and fracture occurred also increased. Additionally, the results from Lehman et al. (2004) indicated that as the aspect ratio increased the maximum lateral displacement increased and the lateral force capacity decreased. The literature review performed indicates that different authors reached similar conclusions with respect to the effects of moment-shear span ratio on column structural performance. However, it should be noted that these similar conclusions were reached for a wide range of scales, shapes, and reinforcement type and amount.

This chapter reports on testing performed on four half-scale circular RC bridge columns. Two pairs of columns were tested and evaluated to determine the effects of reinforcement grade and the effects of the moment-shear span ratio.

6.2 EXPERIMENTAL PLAN

The experimental research plan is shown in **Figure 6.1**. The first pair of columns, denoted G60 and G80, had a moment-shear span ratio equal to six (6). The second pair of columns, denoted G60-s and G80-s, had a moment-shear span ratio equal to three (3). **Figure 6.1** also shows the cross-sections and column dimensions. The column test height, H, is equal to 12 feet (3.66 m) for the first pair of columns (G60 and G80) and equal to 6 feet (1.83 m) for the second pair of columns (G60-s and G80-s). All columns tested were 2-feet (0.61 m) in diameter, which correspond to half-scale specimens of a typical 4-foot (1.22 m) diameter column built in

the western US, including California (Schoettler et al. 2012), Oregon, and Washington as well as in Japan (Kawashima et al. 2009). The column height, diameter, clear cover, and maximum size aggregate (MSA) were scaled while all other dimensions were designed/spaced according to applicable code requirements. The total weight of test specimens, including the RC load stub and footing, was 10.45 tons (9.48 metric tonnes) for the taller columns and 9.04 tons (8.20 metric tonnes) for the shorter columns.

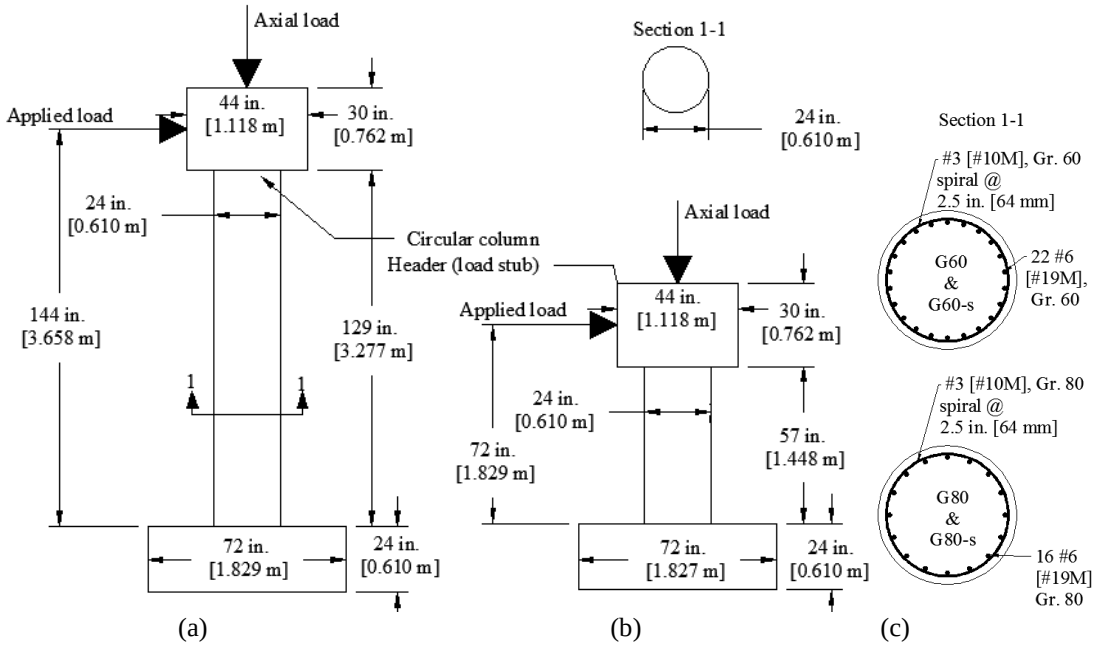

Figure 6.1 Specimen Geometry of: (a) Columns G60 & G80 and (b) Columns G60-s & G80-s; (c) Column Cross-Section Detailing.

Columns G60 and G60-s were designed with a longitudinal reinforcement ratio of ρ_l = 2.19 percent corresponding to 22 #6 (22 ø19 mm) Grade 60 [420] reinforcing bars. Columns G80 and G80-s have a longitudinal reinforcement ratio of ρ_l = 1.58 percent corresponding to 16 #6 (16 ø19 mm) Grade 80 [550] HSS reinforcing bars. **Figure 6.2** illustrates the stress-strain plots for three Grade 60 and three Grade 80 reinforcement bar specimens. Columns G80 and G80-s

were designed to provide approximately the same moment capacity as columns G60 and G60-s, but were constructed with Grade 80 [550] reinforcement. Note that the increase in the ratio of nominal yield strength does not perfectly match the decrease in the ratio of the number of longitudinal reinforcing bars. The increase in nominal yield strength ratio was 1.33 (80/60) and the decrease in the number of longitudinal bars was 1.38 (22/16). All four columns have the same spiral pitch of 2.50 inches (63.5 mm) and have 1.25 inches (31.8mm) of clear cover. The spiral reinforcement bar size is #3 (ø10 mm) for all columns. The pitch and bar size corresponds to a transverse reinforcement ratio of ρ_t = 0.82 percent. The column transverse and longitudinal reinforcement were extended into the footing as required by Oregon Department of Transportation Bridge Design and Drafting Manual (ODOT, 2012) and AASHTO applicable code requirements. The concrete mixture contained a ⅜-inch (9.5 mm) (MSA). The concrete mixture was also proportioned to be pumpable and had a minimum required slump of 5 inches (127 mm). The reported concrete unit weight was 142 lb/ft^3 (22.5 kN/m^3). Concrete strengths listed in Table 1 are obtained from concrete cylinder testing performed during the day of column testing. At least 3 samples were tested for each type of test for each column.

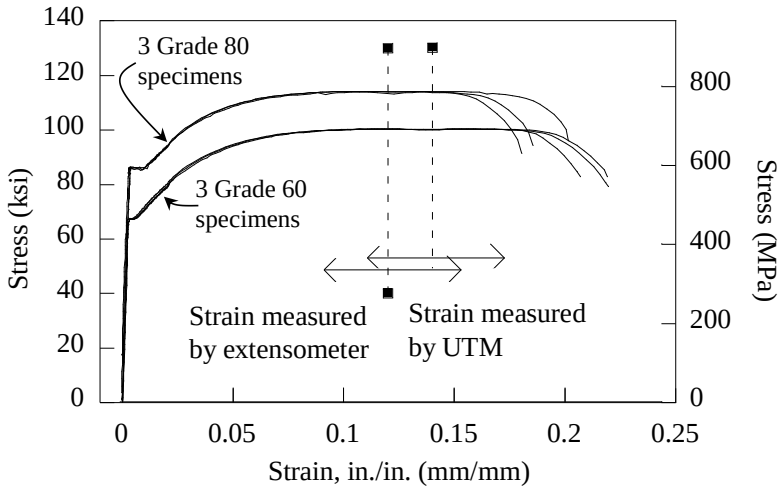

Figure 6.2 Stress-strain plot of ASTM A706 Grade 60 #6 and Grade 80 #6 (ϕ19 mm) reinforcing bars.

6.2.1 Construction Sequence

Concrete casting was performed with two placements for each pair of columns, which were cast with the same batch of concrete on the same day to reduce variability in the material. First, the footing was cast, and then the columns and load stubs were cast a week later. Due to physical constraints of the laboratory, each pair of columns was not tested on the same day, which helps explains the difference in concrete strengths at day of testing listed in Table 6.1.

6.2.2 Instrumentation

Each test column was instrumented to quantify indicators of column performance during cyclic testing. **Figure 6.3** shows the external instrumentation and experimental setup. To measure curvatures and displacements at different locations in the columns, instrumentation were installed at various locations along the height of the columns. In total, 78 sensors were installed for taller columns and 75 sensors were installed for the shorter columns, including 29 strain gages that were placed on both the longitudinal (22 strain gages) and transverse (7 strain gages) reinforcement for all columns (not shown in figure).

Two ⅜-inch (9.5 mm) diameter threaded rods were cast with the concrete column at four different elevations for columns G60-s and G80-s and five different elevations for columns G60 and G80 (elevations are shown in **Figure 6.3**(b) and **Figure 6.3** (a), respectively). Aluminum angles were attached to the threaded rods. At least sixteen string potentiometers, labeled B in **Figure 6.3**, (two on each aluminum angle) were attached to the aluminum angles to obtain measurements to determine the column curvatures. **Figure 6.3** also shows the locations of the string potentiometers and additional instrumentation for columns G60-s and G80-s. Note that the locations of the bottom three levels are identical for columns G60 and G80. A load cell within the actuator, labeled G in **Figure 6.3a and 6.3b**, was used to measure the applied horizontal load and one string potentiometer, labeled A in **Figure 6.3a and 6.3b**, was used to measure the tip displacement. Details on additional instrumentation can be found in Trejo et al. (2014).

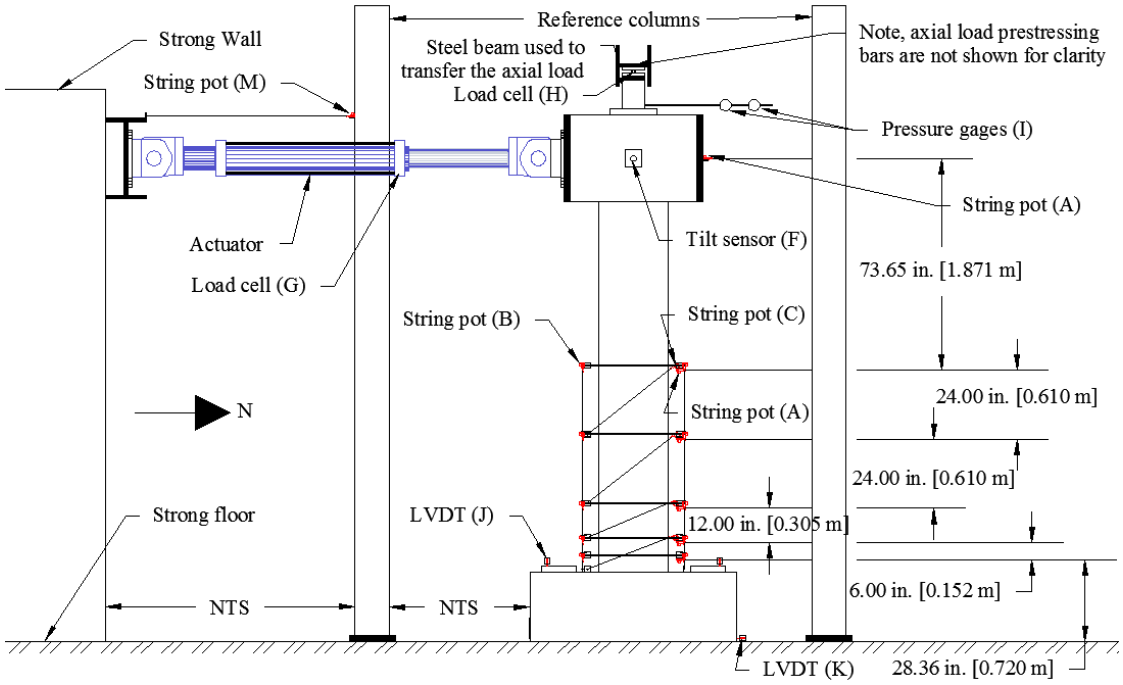

(a)

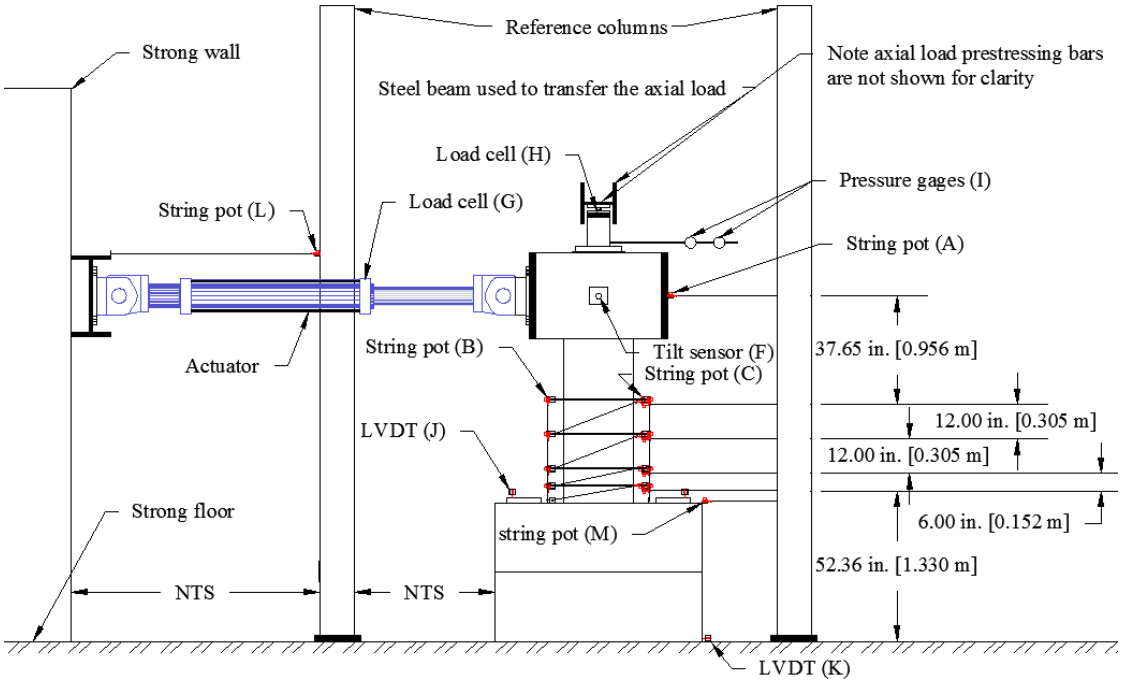

(b)

Figure 6.3 External Instrumentation for Columns: (a) G-60 & G-80, and (b) G60-s & G80-s (NTS – not to scale).

6.2.3 Test Setup and Testing Procedure

Test setup initiated with stressing the column footing to the strong floor. For the second pair of columns (G60-s and G80-s) a RC spacer block was placed between the bottom of the column footing and the strong floor. The hydraulic actuator was then bolted to the RC load stub and the axial load system was assembled. The axial load was applied with a hydraulic jack located between the top of the load stub and a steel reaction beam. The steel reaction beam (6-feet [1.83 m] W12x152) was connected to the column footing using prestressing threaded rods. A concave plate and convex nut were used at the base to allow for rotation of the prestressing rod. The top load transfer beam was supported on a large diameter hydraulic hollow jack and load cell, which aligned the axial load with the specimen as it deformed. In addition to the large diameter hydraulic jack, a pneumatic nitrogen accumulator was placed in series with the jack to reduce variations of the pressure in the hydraulic system and applied axial load. The applied axial load was 90 kips (400 kN), corresponding to five percent of the nominal axial capacity of the column in compression.

Table 6.2 lists the testing protocol and **Figure 6.4** shows the profile in terms of drift ratio versus the number of cycles. Horizontal loading consisted of pushing and pulling the column (in the north-south direction) to predetermined drift ratio levels. Each drift ratio level consisted of three cycles (six peaks): each cycle started at zero displacement, was then displaced in the positive direction towards the positive peak (North), was then displaced in the negative direction towards the negative peak (South), and was then returned back to zero displacement. This process was repeated three times for each predetermined drift ratio level. Both pairs of columns were tested to the same drift ratio levels. Thus, to achieve the same drift ratios the tip

displacements of the second pair of columns (G60-s and G80-s) were half of the tip displacements of the first pair of columns (G60 and G80).

Table 6.2 Loading profile of columns G60, G80, G60-s, and G80-s.

Drift ratio cycle, %	Number of cycles	Loading rate, in/s (mm/s)	
		G60 & G80	G60-s & G80-s
0.1	3	0.01 (0.25)	0.005 (0.13)
0.2	3	0.01 (0.25)	0.005 (0.13)
0.3	3	0.01 (0.25)	0.005 (0.13)
0.5	3	0.01 (0.25)	0.005 (0.13)
0.7	3	0.01 (0.25)	0.005 (0.13)
0.9	3	0.02 (0.51)	0.01 (0.25)
1.7	3	0.04 (1.0)	0.02 (0.51)
2.6	3	0.08 (2.0)	0.04 (1.0)
3.5	3	0.08 (2.0)	0.04 (1.0)
4.3	3	0.08 (2.0)	0.04 (1.0)
5.2	3	0.08 (2.0)	0.04 (1.0)
6.1	3	0.08 (2.0)	0.04 (1.0)
6.9	3	0.16 (4.1)	0.08 (2.0)

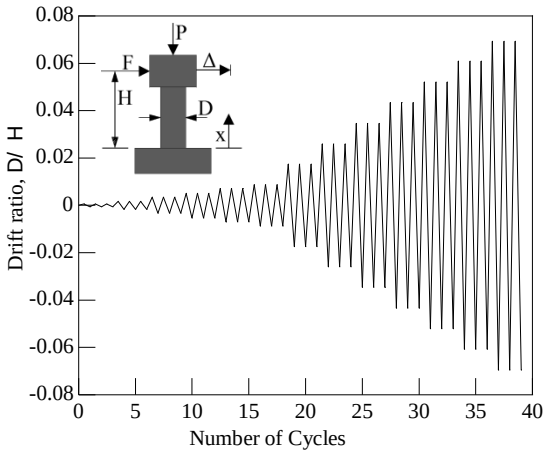

Figure 6.4 Loading Profile of Columns G60, G80, G60-s, and G80-s.

Table 6.3 summarizes the tensile testing performed on the reinforcing steel bars. Details on the material testing results can be found in Trejo et al. (2014) and can be provided by the corresponding author upon request. The material properties of the concrete and steel reinforcement used, several material tests were performed. Concrete material testing included compressive strength tests (ASTM C39), splitting tensile strength tests (ASTM C496), modulus-of-elasticity tests (ASTM C469), and modulus-of-rupture tests (ASTM C78). Concrete samples were made and cured following ASTM C31 specifications. The reinforcement characteristics were obtained from tension tests performed using a 110-kip (489 kN) universal testing machine following ASTM E8, E83, and A370 specifications.

Table 6.3 Summary of tensile testing results for the reinforcing steel bar

Bar size	Grade, ksi (MPa)	Yield point* (0.2% offset)		Tensile strength		Ultimate strain		Elong. % in 8 inch (203 mm)
		Stress, ksi (MPa)	Strain, in./in. (mm/mm)	Stress, ksi (MPa)	Strain, in./in. (mm/mm)	Stress, ksi (MPa)	Strain, in./in. (mm/mm)	
#3 (#10M)	Gr. 60 (420)	72.8 (502)	0.0045	102.1 (704)	0.1185	73.2 (505)	0.1571	15
#5 (#16M)	Gr. 60 (420)	66.7 (460)	0.0046	93.7 (646)	0.1310	71.8 (495)	0.1982	17
#6 (#19M)	Gr. 60 (420)	67.2 (463)	0.0043	100.1 (690)	0.1402	81.5 (562)	0.2155	16

#3 (#10M)	Gr. 80 (550)	85.6 (590)	0.0055	120.5 (831)	0.0947	85.2 (588)	0.1378	13
#5 (#16M)	Gr. 80 (550)	86.2 (594)	0.0051	114.3 (788)	0.1066	86.8 (598)	0.1555	14
#6 (#19M)	Gr. 80 (550)	86.1 (593)	0.0048	114.0 (786)	0.1225	93.9 (647)	0.1893	15

* The yield point is defined as intersection of the 0.2 percent offset line and stress-strain curve

6.3 TEST RESULTS AND DISCUSSION

Test results of the two pairs of columns (G60 and G80, G60-s and G80-s) were compared to determine the effects of the steel reinforcement grade and the effect of moment-shear span ratio on column performance. Steel reinforcement strains, column capacity, column ductility, and energy dissipation are compared in this paper. It is worth noting that all four columns exhibited flexural failure, in which longitudinal reinforcing bar buckling followed by longitudinal reinforcing bar fracture was the main mode of failure. Failure of the columns was defined at the point when the first longitudinal reinforcing bar facture occurred. Observations of column damage progression and post-failure column performance are also discussed.

6.3.1 Steel Reinforcement Strains

The drift at which the first longitudinal reinforcing bar yielded in the columns is presented in this paragraph. The longitudinal reinforcement in column G60-s initially yielded at a drift ratio of 0.69 percent (-0.50 inches, -13 mm) and was measured at a location at 12 inches (305 mm) from the base of the column (level 4). The longitudinal reinforcement in column G80-s initially yielded at a tip displacement of -0.56 inches (-14 mm), which corresponds to a drift ratio of 0.78 percent. This value was recorded at a distance 6 inches (152 mm) above the base of the column (level 3). The longitudinal reinforcement in column G60 initially yielded at a tip displacement of 1.44 inches (36.6 mm), which corresponds to a drift ratio of 1.00 percent. This occurred during the approach to the first peak of the 1.7 percent drift ratio cycle at the base of the

column (level 2). Also at level 2, the longitudinal reinforcement in column G80 initially yielded during the 1.7 percent drift ratio cycle, at 1.58 inches (40.1mm) of displacement corresponding to 1.1 percent drift ratio. When comparing columns G80-s and G80, column G80 exhibited two more drift ratio cycles prior to the longitudinal reinforcement yielding. This result was similar to the difference between columns G60 and G60-s. Results indicate that as the yield strength of the reinforcing steel was increased the drift ratio at which yielding occurred also increased. For both moment-shear span ratios, the increase in the drift at which first yield was observed is equal to 10%. As the moment-shear span ratio is increased the yield drift also increases. This increase was similar for both the control (Grade 60) columns and the Grade 80 [550] HSS columns.

Inelastic strains in the longitudinal reinforcement of plastic hinges reach peak values at the column ends, and penetrate into the footing. As the tensile stress in the reinforcement is transferred to the footing, through bond stresses along the reinforcement, the strain incompatibility between the reinforcement and surrounding concrete in the footing results in bond-slip. Bond-slip develops along most of the anchorage length of the bar into the footing. Assuming that the reinforcement is well anchored, the bond-slip can be estimated based on the accumulation of strains in the reinforcement, and therefore estimated by integrating the tension reinforcement strain profile. While strain penetration also occurs in the steel and concrete when in compression, it is minimal and often disregarded. Strain penetration can be estimated by integrating the tension reinforcement strain profile below the base of the column. Thus, towards understanding the effects of steel grade and moment-shear span ratio on the strain penetration, the measurements of the strains at level 1 (inside the footing) are presented next. At strain gage level 1 (inside the footing), column G60 initially yielded on the 2.6 percent drift ratio cycle while column G60-s initially yielded on the 1.7 percent drift ratio cycle. The longitudinal

reinforcement in column G80-s yielded at 0.78 percent drift ratio and the longitudinal reinforcing bars in column G80 never yielded in the footing. Test data show that the columns constructed with Grade 80 [550] HSS reinforcement exhibited the maximum strains in the longitudinal reinforcement further above the base of the column when compared to the columns constructed with Grade 60 [420] reinforcement.

6.3.2 Column Capacity

Table 6.4 summarizes the results of testing in terms of columns forces and overstrength factors. Column forces reported include maximum column shear force and maximum tested moment capacity. It is worth noting that the column shear forces have been computed from applied forces accounting for geometry effects of the applied axial. **Table 6.4** also lists two overstrength factors. First, the static nominal overstrength factor, defined as the ratio of the tested moment capacity to the nominal moment capacity. Second, the static plastic overstrength factor is presented, which corresponds to the ratio of the tested moment capacity to the plastic moment capacity obtained using measured material properties. Both nominal and plastic moment capacities are computed using Response 2000. The plastic overstrength factors are obtained following the AASHTO Guide Specifications LRFD Seismic Bridge Design (2011). Columns G60/G60-s and columns G80/G80-s have static nominal overstrength values of 1.36 and 1.28, respectively. This indicates that: (i) columns constructed with Grade 80 reinforcement develop smaller overstrength factors due to the presence of smaller reinforcement ratios, and (ii) the moment-shear span ratio does not significantly affect the computed overstrength factor. The reported values for the plastic overstrength factor are 1.28/1.27 and 1.20/1.22 for columns G60/G60-s and G80/G80-s, respectively. The values for the Grade 80 columns are all lower than the values achieved by Grade 60 columns. However, it should be noted that these values are

slightly larger than the AASHTO value of 1.2 that also considers other phenomena not simulated in these tests, such as other sources of kinematic overstrength, dynamic amplification, and rheological effects, which would suggest that the value of 1.2 may conservatively underestimate the true capacity. Therefore, based on these testing results, it is suggested that the AASHTO value of 1.2 remain unchanged for columns constructed with HSS reinforcement.

Table 6.4 Columns G60, G80, G60-s, and G80-s Capacities and Overstrength Factors.

Column	Maximum shear force *kip* (kN)	Nominal moment capacity, M_n *kip-ft* (kN-m)	Plastic moment capacity, M_p *kip-ft* (kN-m)	Tested moment capacity, M_T *kip-ft* (kN-m)	Static$^{\alpha}$ nominal overstrength factor, $\lambda_1 = M_T/M_n$	Static$^{\alpha}$ plastic overstrength factor, $\lambda_2 = M_T/M_P$
G60	*47.9* (213)	*463* (628)	*493* (665)	*631* (856)	1.36	1.28
G80	*43.1* (192)	*448* (607)	*480* (651)	*572* (776)	1.28	1.20
G60-s	*100.4* (446.6)	*463* (628)	*495* (671)	*629* (853)	1.36	1.27
G80-s	*92.0* (409.2)	*448* (608)	*469.2* (636)	*575* (780)	1.28	1.22

$^{\alpha}$ dynamic amplification and kinematic overstrength factors not considered due to quasi-static nature of testing

Figures 6.5a and 6.5b show the shear force versus drift ratio of columns G60 and G80 and of columns G60-s and G80-s, respectively, up to the first longitudinal reinforcement fracture. It can be seen that there are slight differences in the peak strength capacity. The difference in the maximum shear force was expected because the nominal moment capacities of the columns were different since the increase in yield strength of the longitudinal reinforcement did not match exactly the reduction in the area of the longitudinal reinforcement. It can be seen that the overall shape of the hysteretic loops are similar, but the columns reinforced with Grade 60 reinforcement exhibited slightly larger shear forces, as well as slightly stiffer initial loading and unloading curves, resulting in greater energy dissipation compared to the Grade 80 columns.

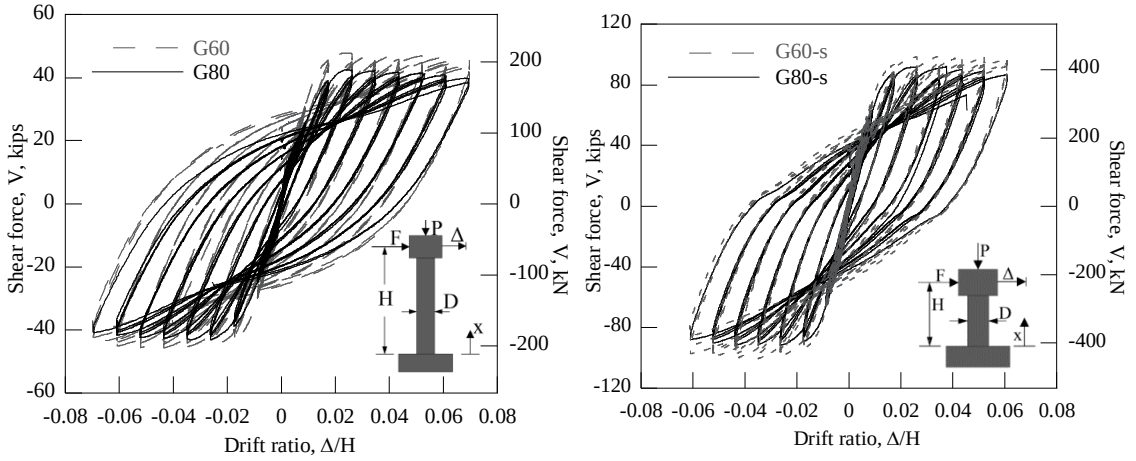

(a) (b)

Figure 6.5 Shear Force versus Drift Ratio of Columns: (a) G60 & G80, and (b) G60-s & G80-s.

Figures 6.6a and 6.6b show the shear force versus drift ratio up to the first fracture of longitudinal reinforcement for columns G60 and G60-s and for columns G80 and G80-s, respectively. These figures indicate that the shear force in the shorter columns (G60-s and G80-s) are approximately twice the shear force of the taller columns (G60 and G80). This is expected due to the shorter columns having half the moment-shear span ratio of the taller columns. However, the taller columns (G60 and G80) exhibited larger drift ratios prior to failure when compared to the shorter columns (G60-s and G80-s). It is also worth noting that the shorter columns are also considerably stiffer than the taller columns.

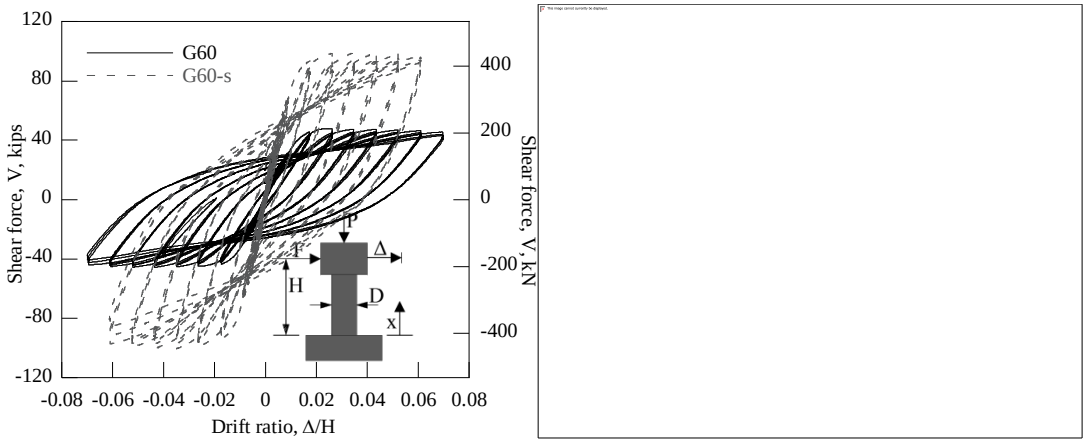

(a) (b)

Figure 6.6 Shear Force Versus Drift Ratio: (a) G60 & G60-s (b) G80 & G80-s.

Finally, it should be noted that all four columns were well detailed. Thus, for the tested aspect ratios and shear forces were not expected to cause column failure, even for the relatively short columns with a moment-shear span ratio of 3. However, these results may not be extended to columns with larger longitudinal reinforcement ratios or larger axial load rations, as undesired compression failure of the core may govern the failure. Future testing addressing the last two points are needed before generalization of the results shown above is possible.

6.3.3 Column Ductility

Column ductility is defined here for both displacement and curvature. Displacement ductility is computed as the ratio of the maximum absolute tip displacement to the tip displacement at a reference yield displacement of the column. The reference yield of the column is defined herein in two ways: (i) based on the definition of reference yield curvature by Priestley et al. (2007), which is summarized below for completeness of this paper; and (ii) and based on the curvature distribution at a point when first yield of the column longitudinal reinforcement was measured in the longitudinal strain gages attached to the reinforcing bars.

Table 6.5 provides a summary of the displacement and curvature ductility values. The displacement ductility demand values based on the reference yield by Priestley et al. (2007) are larger for columns G60/G60-s when compared to the columns G80/G80-s. This is mainly due to larger nominal yield values used in estimation of the yield curvature in Equation 1, and to a smaller extent to the larger estimate of the strain penetration used in Equation 3. Nonetheless, similar peak drift ratios were achieved for both taller and shorted pairs of columns. Column G60-s exhibited significantly larger curvature ductility values at the curvature instrumentation levels 1, 3 and 4 when compared to column G80-s. However, column G80-s exhibited a significantly

larger curvature ductility value at curvature instrumentation level 2, 12 inches (305mm) above the base of the column, when compared to column G60-s. The curvature ductility is typically more critical towards the base of the column where the majority of the curvature occurs. In this case, the data indicates that the curvature ductility value of column G60-s is greater than column G80-s at the base of the column (level 1) where strain penetration effects also influence the value. However, at level 2 where strain penetration effects do not affect the curvature ductility value, column G80-s exhibited larger curvature ductility values when compared to column G60-s, which can also be related to the larger development length of the Grade 80 [550] HSS reinforcement.

Columns G60-s and G80-s exhibited larger displacement ductility values when using the reference yield and first yield criteria compared to column G60 and G80, respectively. This suggests the decrease in moment-shear span ratio results in larger displacement ductility values. However, for curvature ductility values not influenced by strain penetration effects (levels 2, 3, and 4) the decrease in the moment-shear span ratio decreases the curvature ductility demands.

Table 6.5 Ductility Demand of Columns G60, G80, G60-s, and G80-s.

Specimen	Displacement ductility, μ_Δ		Curvature ductility, μ_ϕ			
	Reference Yield [α]	First Yield	Level 1	Level 2	Level 3	Level 4
G60	5.93	7.00	20.89	19.16[χ]	6.63	2.32
G80	4.69	6.33	23.63	10.21	5.61	1.54
G60-s	9.46	8.88	33.31	7.14	4.46	0.91
G80-s	7.33	7.80	26.86	8.38	2.45	0.74

[α] Computed following Priestley et al. (2007)

χ This large value is believed to have occurred due to the excessive deep spalling on the south side of the column reducing the compressive resistance of the column resulting in larger curvature in this region. It should also be noted this value occurred on the final peak of the 10.00-inch (254mm) displacement cycle shortly prior to column failure.

6.3.4 Energy Dissipation

The energy dissipated by each column was determined by numerical integration using the Simpson rule on the applied force over displacement hysteretic loops for each displacement cycle. The hysteretic energy dissipated, , is given by:

$$E_h = \int F(\Delta)\, d\Delta \qquad (1)$$

where F is the applied horizontal actuator force and Δ is the displacement measured at the same elevation as the applied force F.

Figure 6.7 shows the cumulative energy dissipated up to the first reinforcing bar fracture for the four columns. The shorter columns (G60-s and G80-s) exhibited greater energy dissipation when compared with the taller columns (G60 and G80) prior to the failure drift ratio cycle. This is due to the increase in column stiffness of the shorter columns which resulted in a greater area within the hysteretic loops. The results indicate that a reduction in the moment-shear span ratio results in an increase in energy dissipation capacity after the longitudinal reinforcement has yielded for columns constructed with either Grade 60 [420] or Grade 80 [550] HSS reinforcement. This is believed to be mainly due to the increase in column stiffness. However, it should be noted that the columns with a larger moment-shear span ratio (columns G60 and G80) exhibited larger drift ratios prior to failure, which resulted in an overall increase in energy dissipation capacity at column failure when compared with columns with a smaller moment-shear span ratio (columns G60-s and G80-s).

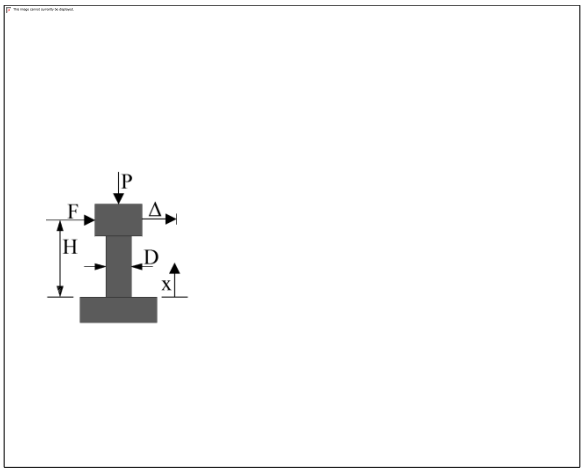

Figure 6.7 Cumulative Energy Dissipation of Columns G60, G80, G60-s, and G80-s.

6.3.5 Damage Progression

The damage progression was similar for all four columns. Damage concentrated near the base of the column, where plastic hinges developed. However, concrete cracks extended throughout the full length of the columns. As shown in Figure 6.8, in all columns, concrete spalling, longitudinal reinforcing bar buckling, and longitudinal reinforcing bar fracture occurred within one column diameter (2 feet or 0.61m) from the base. In the region within one column diameter, flexural cracks were observed for columns G60 and G80 (see Figures 6.8a and 6.8b) while flexure and shear (diagonal) cracks were observed for columns G60-s and G80-s (see Figures 6.8e and 6.8f). Concrete spalling extended further up in the columns with larger moment-to-shear span ratios, and furthest up in column G60. First longitudinal bar fracture occurred after initiation of bar buckling. Necking of the reinforcement was not observed (see Figure 6.8c), which indicates that the longitudinal bar fractures were due to low-cycle fatigue (Mander et al. 1994, Rodriguez et al. 1999). In general, spiral reinforcement did not yield before first longitudinal bar fracture. However, longitudinal reinforcing bar buckling displaced the spiral reinforcement in column G60 (Figure 6.8a), G80 (Figure 6.8b), and G80-s (Figure 6.8f),

thereby increasing the spiral spacing. Initially, bar buckling was observed in the radial direction. However, bar buckling was also observed in the circumferential direction due to concrete crushing of the core near the spiral reinforcing. This bar buckling mode of failure spanned across multiple spirals. In columns G60 and G80, cracking of the footing was observed post testing on the top face of the footing (Figure 6.8d). This is indicative of cone pull out due to strain penetration.

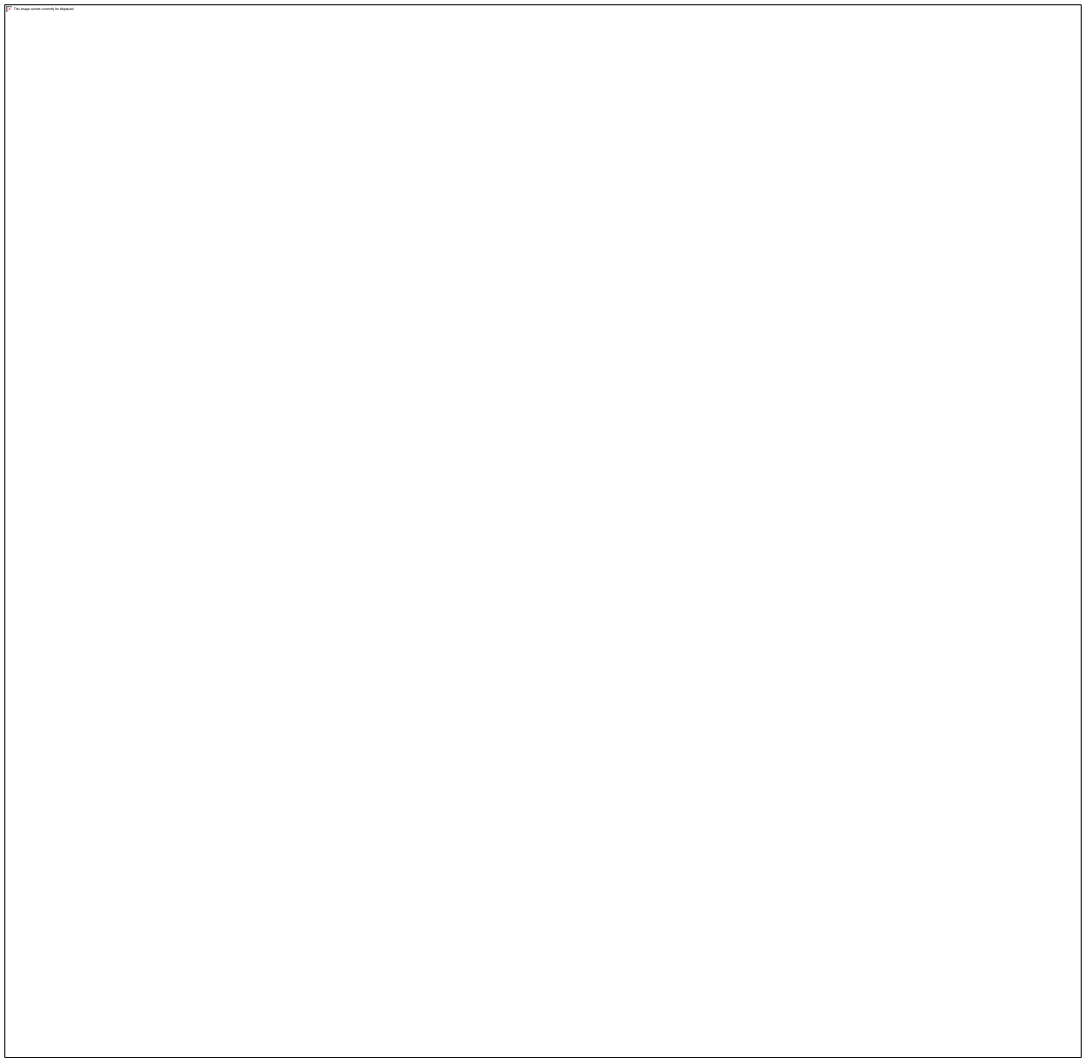

Figure 6.8 (a) Column G60 North Face Post Test, (b) Column G80 North face after first longitudinal bar fracture, (c) Detail of first bar fracture of column G80, (d) Footing crack post test of column G80, (e) Column G60-s post test, (f) Column G80-s post test.

6.4 CONCLUSIONS

The American Society for Testing and Materials (ASTM) currently has a specification for low alloy reinforcing steel (ASTM A706) with a nominal yield strength of 60 ksi (420 MPa) and 80 ksi (550 MPa). However, the American Association of State Highway and Transportation Officials (AASHTO) and specifications for select State Highway Agencies (SHAs) do not allow the use of Grade 80 [550] HSS reinforcement in reinforced concrete compression members designed to form a plastic hinge. This limitation is due to lack of information on the material characteristics of ASTM A706 Grade 80 [550] reinforcement and due to a lack of test data on the cyclic performance of plastic hinges in compression members. The use of Grade 80 [550] HSS reinforcement in RC bridge columns has the potential to reduce reinforcement quantities, reduce reinforcement congestion, and improve constructability, thus making the construction of new bridges more economical. However, limited research has been performed to validate the use of Grade 80 [550] HSS reinforcement, especially in compression members that may develop plastic hinges.

The research presented assessed the performance of two pairs of columns which were subjected to lateral cyclic testing. Each pair consisting of one column constructed with Grade 60 [420] reinforcement and the other constructed with Grade 80 [550] HSS reinforcement. Both pairs of columns were designed to have similar moment capacities, but had different moment-shear span ratios. Columns constructed with Grade 80 [550] HSS reinforcement were designed to have similar moment capacity as the columns constructed with Grade 60 [420] reinforcement. This was achieved by reducing the number of longitudinal reinforcing bars proportionally to the increase in nominal yield strength.

The main conclusions that can be drawn from these test results are:

1. Columns constructed with Grade 80 [550] HSS reinforcement achieved similar resistances when compared with the reference columns constructed with Grade 60 [420] reinforcement. Note that the columns constructed with Grade 80 [550] HSS reinforcement had approximately 75% the amount of longitudinal reinforcement of the columns constructed with Grade 60 [420] reinforcement;
2. All four columns failed due to longitudinal reinforcing bar buckling followed by longitudinal reinforcing bar fracture. This indicates the mode of failure was flexural. It should be noted that all of the columns were very well confined to prevent shear failure and other undesired modes of brittle failure;
3. Columns constructed with Grade 60 [420] reinforcement and columns constructed with Grade 80 [550] HSS reinforcement exhibited similar peak drift ratios. Displacement ductility values were larger than four (4.0) for all columns;
4. Columns constructed with Grade 60 [420] reinforcement typically exhibited larger curvature ductility values;
5. The columns constructed with Grade 60 [420] reinforcement exhibited larger hysteretic energy dissipation than the columns constructed with Grade 80 [550] HSS reinforcement. However, energy dissipation is primarily a function of the amount of longitudinal reinforcement and column stiffness rather than a function of the reinforcement grade;
6. Columns constructed with Grade 80 [550] HSS reinforcement tested in this research exhibited lower overstrength factors than columns constructed with Grade 60 [420] reinforcement; this observation is related to two factors: (i) material overstrength is smaller for Grade 80 reinforcing steel, and (ii) column constructed using the HSS reinforcement had smaller reinforcement ratios.

7. The reduction in the moment-shear span ratio did not affect the overstrength factor for columns constructed with either grade of reinforcement; results indicate that aspect ratio does not affect the overstrength factor for well detailed columns that do not exhibit shear failures.
8. The effects of the moment-shear span ratio were similar for columns constructed with Grade 60 [420] reinforcement and columns constructed with Grade 80 [550] HSS reinforcement. The decrease in the moment-shear span ratio resulted in larger curvature ductility values at the base of the column where the effects of strain penetration affects the curvature values and smaller curvature ductility values at higher elevations where the effects of strain penetration do not affect the curvature;
9. Damage progression was similar for all columns. Concrete spalling, longitudinal bar buckling, and bar fractures, concentrated at the base of the column, within a distance of one column diameter from the base;
10. The post-failure performance of column G80-s constructed with Grade 80 [550] HSS reinforcement exhibited similar to superior performance compared to column G60-s, which was constructed with Grade 60 [420] reinforcement, since the G80-s column was able to achieve one more peak (half a cycle) before the sixth bar fractured.

The results in this study present a promising step towards implementation of Grade 80 [550] HSS reinforcement in the design and construction of RC columns, within the bounds of the variables used in is testing program. Other parameters outside of the range studied in this paper should be evaluated. Those could include larger longitudinal reinforcement ratios, larger axial load ratios, and higher concrete strengths.

CHAPTER 7

COMPARISON OF STRATEGIES

Previous chapters discuss in detail the characteristics of three strategies for increasing seismic resilience, accelerating onsite construction and improving durability of bridge bents. Chapters 2 and 3 discuss the use of precast columns and beams, in combination with cast-in-place drilled shafts. Chapters 4 and 5 discuss the use of concrete-filled steel tubes. Chapters 6 discusses the used of higher-strength reinforcement in reinforced concrete bridge columns.

This chapter compares the most salient characteristics of three strategies with those of conventional cast-in-place, reinforced concrete construction. These characteristics are summarized in tables 7.1 to 7.4. The systems are:

- Conventional Construction (CC)
- Precast Concrete columns and beams (PC)
- Concrete Filled Steel Tubes (CFST)
- High Strength Reinforcement (HSR)

The seismic resiliency of these systems are compared in Table 7.1. All the systems are expected to provide life safety by preventing collapse in the design earthquake. Thus the significant differences among the systems is their abilities to withstand larger earthquakes (e.g. MCE or even larger) and in the extent of expected damage and loss of function. None of the systems as designed have provision for active re-centering, so they should be expected to lead to similar residual displacements.

The CFST system has exceptional axial, shear, and flexural capacity, which makes it advantageous for short columns (i.e. at the bottom of freeway ramps) or for bridges with large eccentric truck loadings that induce large overturning moments. These enhanced properties result

from the optimal placement of the steel on the exterior face of the column, as well as the confinement and reduced cracking of the interior concrete. The steel tube acts to confine the concrete fill, which in turn provides large axial stiffness for functionality performance objectives.

The CFST connections evaluated in this report can sustain large deformations and provide large resistance when subjected to lateral loads. When the ER connection is employed, tube buckling tends to develop at 3% to 4% drift near the column-to-foundation and column-to-cap beam interfaces, however this buckling does not result in a decrease in load carrying capacity. Further, drifts exceeding 8% can be developed before tube tearing develops in the buckled region. The WD connection also provides large strength and deformation capacity. The reinforcing ratio in the connection region can be designed to exceed the plastic capacity of the CFST column, and the dowels can be debonded to increase ductility. Deformation capacities exceeding 12% drift were observed in the experiments.

Despite the advantages of CFST components and the connections presented here, note that the large effective reinforcing ratio of the CFST components (and inherent large flexural capacity) can make it difficult to capacity design elements to develop the capacity of the column during seismic events. This is of particular concern when using the ER connection where the CFST steel extends into the cap beam.

The durability of the three concrete systems (CC, PC and HSR) depend mostly on the quality of the concrete used and its ability to resist shrinkage and other cracking. In that regard, the PC system is likely to be slightly more durable than CC and HSR systems, because of higher level of quality control in the production plant than the construction site. HSR likely leads to less reinforcement (to reduce cost), which implies slightly reduced resistance to shrinkage, but shrinkage is rarely a design concern in reinforced concrete columns.

The durability of the CFST system depends on the protective coating (or the existence of additional sacrificial steel thickness), and on the details adjacent to the connections where ingress of water is most likely. Galvanized steel tubes can also be used in extreme environments where corrosion may be of particular concern. It should be noted that numerous bridge columns have already been encased in steel shells as a retrofit measure.

Table 7.1. Comparison of Seismic Resiliency

Strategy	Considerations
Conventional Construction	• Life safety is ensured by contemporary codes, but damage to concrete and reinforcement is likely in the plastic hinge region. Repair of low damage can be achieved using epoxy injection. • In larger earthquakes, repair of bar buckling or fracture can be expensive and delay the return of the bridge to service. • No provision for active re-centering, so residual displacements depend on the particular ground motion.
Precast Cast Columns and Beams	• Same as CC if geometry and details are the same. • The precast system can be modified to contain pre-tensioning, which has been shown to greatly reduce residual deformations.
Concrete Filled Steel Tubes	• Potentially higher drift capacity than CC. • Smaller diameters than comparable RC columns. • More versatile than precast columns (i.e. easy to vary diameter and length) • High-shear, moment, and axial capacity, which is particularly attractive for columns with large eccentric truck loads or short columns. • Can be difficult to capacity design super-structure components to resist the plastic capacity of the CFST column
High-Strength Column Reinforcement	• Same as CC, but • Bar buckling might occur earlier if the bars were substantially smaller. However, using the same bar sizes and for nominally equal bending moment capacities, bar buckling would likely develop at similar drifts.

Table 7.2. Comparison of Speed of Construction

Strategy	Considerations
Conventional Construction	• Construction Sequence: cast foundation, form column, column steel, cast column, shore and form cap beam, cap beam steel, cast cap beam.
Precast Cast Columns and Beams	• Construction Sequence: place PC column, cast foundation, place cap beam, grout cap beam.
Concrete Filled Steel Tubes	• Construction Sequence: cast foundation with opening for column, place column tube, cast column concrete, (grout opening in foundation), place pc cap beam, concrete/grout cap beam connection. • Note that it is important to keep the structural steel and reinforcing bar trades separate during construction.
High-Strength Column Reinforcement	• Construction Sequence: same as for CC, • Reduced congestion makes highly-reinforced sections easier to build and reduces construction costs relative to CC.

Life cycle costs are difficult to estimate, and will vary significantly depending on whether earthquake repair costs are to be included (i.e., whether an earthquake occurs). In Table 7.4, earthquake repair costs are not included. The life cycle costs also depend on contractor familiarity with the different structural systems, because contractors typically price in any uncertainty associated with new systems.

The material costs for the HSR systems are likely to slightly smaller than for the CC system, but in most bridges, labor costs are more important. It is likely that the reduced congestion will somewhat reduce the labor costs of HSR, in comparison with CC. For the PC

and CFST systems, the material costs may be higher than for CC, but the labor costs are expected to be lower once contractors are familiar with the systems and can gain a time advantage. The CFST system uses a relatively high steel percentage (about 4%, compared with a total of approximately 2% in CC) and tube steel is more expensive than rebar steel per unit weight, however, the tube serves as permanent formwork and avoids the forming costs. More importantly, the PC and CFST systems provide the benefit of reducing the indirect costs associated with construction traffic congestion.

Table 7.3. Comparison of Durability

Strategy	Considerations
Conventional Construction	• Potential for cracking caused by shrinkage and other events.
Precast Cast Columns and Beams	• Same as CC. • Some increase in quality control in plant • Adding pre-tensioning reduces cracking potential.
Concrete Filled Steel Tubes	• Depends on protective coating (e.g. paint) for durability
High-Strength Column Reinforcement	• Crack potential may be slightly worse if less reinforcement is used. Would not likely be an important consideration for columns that are subjected to compressive axial load. • Reduced bar congestion improves concrete vibration and reduces potential voids and other defects that can affect durability

Table 7.4. Comparison of Life Cycle Cost

Strategy	Considerations
Conventional Construction	• Initial cost only, if no earthquake.
Precast Cast Columns and Beams	• Potentially lower initial cost (faster on-site construction). • No repair maintenance costs if no earthquake..
Concrete Filled Steel Tubes	• High material cost for steel tube. • No column reinforcing cage cost • No column formwork cost
High-Strength Column Reinforcement	• Life-cycle cost may be slightly lower, mainly since the reinforcement cost may be slightly lower. • Easier construction due to fewer bar congestions in joints and lap-splices may also reduce initial costs. .

REFERENCES

AASHTO (2009). "LRFD Bridge Design Specifications" 4th ed., American Association of State Highway and Transportation Officials, Washington, DC.

AASHTO (2011). AASHTO Guide Specifications for LRFD Seismic Bridge Design. 2nd ed. American Association of State Highway and Transportation Officials, Washington, D.C..

AASHTO (2012). AASHTO LRFD BRIDGE DESIGN SPECIFICATIONS, Customary U.S. Units. American Association of State Highway and Transportation Officials, Washington, D.C.

AASHTO (2014). *AASHTO LRFD BRIDGE DESIGN SPECIFICATIONS, Customary U.S. Units.* American Association of State Highway and Transportation Officials, Washington, D.C.

AASHTO (2015) "AASHTO LRFD Bridge Design Specification," American Association of State Highway and Transportation Officials, Washington, D.C.

ACI 318 (2011). "Building Code Requirements for Structural Concrete". American Concrete Institute, Farmington Hills, MI.

AISC (2011). Steel Construction Manual. American Institute of Steel Construction, Chicago, IL, 14 edition.

ASTM A1035 / A1035M-14 (2014), Standard Specification for Deformed and Plain, Low-Carbon, Chromium, Steel Bars for Concrete Reinforcement, ASTM International, West Conshohocken, PA, www.astm.org

ASTM A370-14 (2014), Standard Test Methods and Definitions for Mechanical Testing of Steel Products, ASTM International, West Conshohocken, PA, www.astm.org

ASTM A615 / A615M-14 (2014), Standard Specification for Deformed and Plain Carbon-Steel Bars for Concrete Reinforcement, ASTM International, West Conshohocken, PA, www.astm.org

ASTM A706 / A706M-14 (2014), Standard Specification for Deformed and Plain Low-Alloy Steel Bars for Concrete Reinforcement, ASTM International, West Conshohocken, PA, www.astm.org

ASTM C31 / C31M-12 (2012), Standard Practice for Making and Curing Concrete Test Specimens in the Field, ASTM International, West Conshohocken, PA, www.astm.org

ASTM C39 / C39M-14a (2014), Standard Test Method for Compressive Strength of Cylindrical Concrete Specimens, ASTM International, West Conshohocken, PA, 2014, www.astm.org

ASTM C469 / C469M-14 (2014), Standard Test Method for Static Modulus of Elasticity and Poisson's Ratio of Concrete in Compression, ASTM International, West Conshohocken, PA, 2014, www.astm.org

ASTM C496 / C496M-11 (2004), Standard Test Method for Splitting Tensile Strength of Cylindrical Concrete Specimens, ASTM International, West Conshohocken, PA, www.astm.org

ASTM C78 / C78M-10e1 (2010), Standard Test Method for Flexural Strength of Concrete (Using Simple Beam with Third-Point Loading), ASTM International, West Conshohocken, PA, www.astm.org

ASTM E8 / E8M-13a (2013), Standard Test Methods for Tension Testing of Metallic Materials, ASTM International, West Conshohocken, PA, www.astm.org

ASTM E83-10a (2010), Standard Practice for Verification and Classification of Extensometer Systems, ASTM International, West Conshohocken, PA, www.astm.org

ATC-24 (1992). "Guidelines for Testing Steel Components". Applied Technology Council, Redwood City, CA.

Berry, M. P., and Eberhard, M.O. (2005). "Practical Performance Model for Bar Buckling." ASCE Journal of Structural Engineering, 131(7):1060-70.

Berry, M. P., and Eberhard, M.O. (2008). "Performance Modeling Strategies for Modern Reinforced Concrete Bridge Columns". PEER Report 2007/07. Pacific Earthquake Engineering Research Center.

Brown, N.K., Kowalsky, M., and Nau, James. (2013). Strain Limits for Concrete Filled Steel Tubes in AASHTO Seismic Provisions. *North Carolina State University*. Report Number FHWA-AK-RD-13-05.

Building Seismic Safety Council for the FEMA. (2004) "NEHRP Recommended Provisions for Seismic Regulations and for New Buildings and Other Structures (FEMA 450) 2003 Ed.," Washington D.C.

Caltrans, (2013). "Seismic Design Criteria Version 1.6," California Department of Transportation.

Chronister, A. (2007). “Experimental Investigation of High Strength Concrete Filled Steel Tubes in Embedded Column Base Foundation Connections.” Unpublished data , University of Washington, Seattle, WA.

Concrete Reinforcing Steel Institute. (2001). “Evaluation of Reinforcing Bars in Old Reinforced Concrete Structures”. Engineering Data Report 48.

Gustafson, D.P. (2010). “Raising the Grade.” Concrete International 32 (04): 59–62.

Haraldsson, O. (2011). “Spread Footing Socket Connections for Precast Columns.” Master’s Thesis, University of Washington, Seattle, WA.

Haraldsson, O.S., Janes, T.M., Eberhard, M.O., and Stanton, J.F. (2013). “Seismic Resistance of Socket Connection between Footing and Precast Column.” Journal of Bridge Engineering, ASCE, Sept-Oct, pp. 910-919.

Janes, T. (2011). “Precast Column Socket Connections for Thin Spread Footings.” Master’s Thesis, University of Washington, Seattle, WA.

Kawashima, K., Sasaki, T., Kajiwara, K., Ukon, H., Unjoh, S., Sakai, J., Kosa, K., Takahashi, Y., Yabe, M., and Matsuzaki, H. (2009). “Shake table experiment on RC bridge columns using E-Defense.” Proc. 41st Panel on Wind and Seismic Effects, UJNR, Public Works Research Institute, Tsukuba Science City, Japan.

Kingsley, A. (2005). “Experimental and Analytical Investigation of Embedded Column Base Connections for Concrete Filled High Strength Steel Tubes.” a thesis submitted in partial fulfillment of Master of Science in Civil Engineering, University of Washington, Seattle, WA.

Lee, J. (2011) “Experimental investigation of Embedded Connections for Concrete Filled Tube Column Connection to Combined Axial-Flexural Loading,” a thesis submitted in partial fulfillment of the degree of Master of Science in Cicil Engineering, University of Washington, Seattle, WA.

Lehman, D., Moehle, J., Mahin, S., Calderone, A., and Henry, L. (2004). “Experimental Evaluation of the Seismic Performance of Reinforced Concrete Bridge Columns.” ASCE Journal of Structural Engineering 130 (6): 869–79.

Lehman, D.E. and Roeder, C.W. (2012) Foundation Connection for Circular Concrete Filled Tubes, *Journal of Constructional Steel Research,* Vol. 78, November 2012, pgs. 212-25, Elsevier.

Li, Y.A., Huang, Y.T., and Hwang, S.J. (2014). "Seismic Response of Reinforced Concrete Short Columns Failed in Shear." ACI Structural Journal 111 (1-6).

Mander, J., Panthaki, F., and Kasalanati, A. (1994). "Low-Cycle Fatigue Behavior of Reinforcing Steel." Journal of Materials in Civil Engineering 6 (4): 453–68.

McLean, D.I. and Smith C.L. (1997), "Noncontact Lab Splices in Bridge Column-Shaft Connections," Washington State Department of Transportation Report WA-RD 417.1, Olympia, Washington, July.

Montejo, L., Kowalsky, M., and Hassan, T. (2009). Seismic Behavior of Flexural Dominated Reinforced Concrete Bridge Columns at Low Temperatures, *Journal of Cold Regions Engineering*, Vol. 23, pp. 18-42.

ODOT (2012). "Oregon Department of Transportation Bridge Design and Drafting Manual," rev. August 2012. Oregon Department of Transportation, 2012, URL: http://www.oregon.gov/odot/hwy/bridge/Pages/standards_manuals.aspx#Bridge_Design_&_Drafting_Manual (accessed Dec. 4, 2012)

Pang, J.B.K., Steuck, K.P., Cohagen, L.S., Eberhard, M.O. and Stanton, J.F. (2008), "Rapidly Constructible Large-Bar Precast Bridge-Bent Connection," Washington State Department of Transportation Draft Report, WA-RD 684.2, Olympia, Washington, October, 184 pp.

Pham, T.P., and Li, B. (2014). "Seismic Performance of Reinforced Concrete Columns with Plain Longitudinal Reinforcing Bars." ACI Structural Journal 111 (3): 561–72.

Priestley, M.J.N., Calvi, G.M., and Kowalski, M.J. (2007). "Displacement-based Seismic Design of Structures." IUSS Press, Pavia, Italy

Rautenberg, J.M., Pujol, S., and Lepage, A. (2010). "Cyclic Response of Concrete Columns Reinforced with High-Strength Steel." 9th US National and 10th Canadian Conference on Earthquake Engineering, Including Papers from the 4th International Tsunami Symposium 3. Accessed May 29, http://nees.org/resources/679/download/2010EQConf-000996.PDF.

Restrepo, J. I., Tobolski, M.J., and Matsumoto, E.E. (2011). *Development of a Precast Bent Cap System for Seismic Regions*. NCHRP Report 681.

Rice, P., and Gustafson, D. (1976). "Grade 80 [550] Reinforcing Bars and ACI 318-71." ACI Journal Proceedings 73 (4): 199–206.

Risser, R., and Hoffman, M. (2014). "Turning Billets into Bars." Concrete Construction. Accessed May 29, 2014. http://www.concreteconstruction.net/rebar/turning-billets-into-bars.aspx.

Rodriguez, M., Botero, J., and Villa, J. (1999). "Cyclic Stress-Strain Behavior of Reinforcing Steel Including Effect of Buckling." Journal of Structural Engineering 125 (6): 605–12.

Roeder, C.W., Cameron, B., and Brown, C.B., (1999) Composite action in concrete filled tubes, *Structural Engineering*, ASCE, Vol 125, No. 5, May 1999, pp. 477-84.

Roeder, C.W, Lehman, D.E., and Thody, R. (2009) Composite Action in CFST Components and Connections, *AISC Engineering Journal*, AISC, Vol 46, No. 4, pp. 229-42.

Roeder, C.W., Lehman, D.E., and Bishop, E. (2010). Strength and Stiffness of Circular Concrete Filled Tubes, *ASCE Journal of Structural Engineering*, Vol 135, No. 12, pgs 1545-53, Reston, VA.

Schoettler, M., Restrepo, J.I., Guerrini, G, Duck, D.E., Carrea, F. (2012), "A Full-Scale, Single-Column Bridge Bent Tested by Shake-Table Excitation.", Center for Civil and Engineering Earthquake Research, Department of Civil Engineering/258, University of Nevada, Reno, Accessed May 29, 2014. https://nees.org/resources/6868.

Stephens, M.T., Lehman, D.E, and Roeder, C.W. (2015). Concrete-Filled Tube Bridge Pier Connections for Accelerated Bridge Construction. Technical Report CA15-2417, California Department of Transportation.

Tran, H.V. (2015). "Drilled Shaft Socket Connections for Precast Columns in Seismic Regions." PhD Thesis, University of Washington, Seattle, WA.

Trejo, D., Barbosa, A.R., and Link, T. (2014). "Seismic Performance of Circular Reinforced Concrete Bridge Columns Constructed with Grade 80 [550] Reinforcement." Research SRS 500-610, Report No. FHWA-OR-RD-15-02. Oregon State University. URL: http://www.oregon.gov/ODOT/TD/TP_RES/docs/Reports/2014/14RS0500_610_SeismicReportFinal.pdf (accessed Nov. 4, 2014)

WSDOT BDM (2012). "Bridge Design Manual (LRFD)", Washington State Department of Transportation, Olympia, Washington, August.

Yeh, I.C. (2006). "Generalization of Strength versus Water–cementitious Ratio Relationship to Age." Cement and Concrete Research 36 (10): 1865–73. doi:10.1016/j.cemconres.2006.05.013.